

Diagnostics of Eddy Mixing in a Circumpolar Channel

Ryan Abernathey^a, David Ferreira^b, Andreas Klocker^c

^a*Scripps Institution of Oceanography*

^b*Massachusetts Institute of Technology*

^c*The Australian National University, Canberra, ACT, Australia and the Australian Research Council Center of Excellence for Climate System Science*

Abstract

Mesoscale eddies mix tracers horizontally in the ocean. This paper compares different methods of diagnosing eddy mixing rates in an idealized, eddy-resolving model of a channel flow meant to resemble the Antarctic Circumpolar Current. The first set of methods, the “perfect” diagnostics, are techniques suitable only to numerical models, in which detailed synoptic data is available. The perfect diagnostic include flux-gradient diffusivities of buoyancy, QGPV, and Ertel PV; Nakamura effective diffusivity; and the four-element diffusivity tensor calculated from an ensemble of passive tracers. These diagnostics reveal a consistent picture of along-isopycnal mixing by eddies, with a pronounced maximum near 1000 m depth. The only exception is the buoyancy diffusivity, a.k.a. the Gent-McWilliams skew diffusivity, which is weaker and peaks near the surface and bottom. The second set of methods are observationally “practical” diagnostics. They involve monitoring the spreading of tracers or Lagrangian particles in ways that are plausible in the field. We show how, with sufficient ensemble size, the practical diagnostics agree with the perfect diagnostics in an average sense. We then demonstrate how the practical diagnostics can be used to reconstruct the dynamically important eddy fluxes using diffusive closures.

Keywords: mesoscale eddies, eddy diffusivity, isopycnal mixing, Antarctic Circumpolar Current

¹ 1. Introduction

² The meridional overturning circulation (MOC) of the ocean plays a fun-
³ damental role in the climate system by providing a link between the deep

4 ocean, where vast quantities of heat and carbon can be stored, and the atmo-
5 sphere (Sarmiento and Toggweiler, 1984; Sigman and Boyle, 2000; Marshall
6 and Speer, 2012). Despite its importance, direct observation of the MOC is
7 extremely challenging, demanding continuous, high-resolution measurements
8 of the ocean flow field across entire basins and through the full water col-
9 umn. One such attempt has been made in the North Atlantic through the
10 RAPID program, a dense array of moorings and repeat sections along 26.5°
11 N (Bryden et al., 2005; Cunningham et al., 2007). However, doubt remains
12 whether even this sophisticated network can distinguish MOC trends from
13 slow internal variability and noise from the eddy field (Wunsch, 2008). Given
14 the size, remoteness, and hostility of the Southern Ocean, it seems unlikely
15 that such direct approaches will be implemented there in the foreseeable fu-
16 ture. Instead, various indirect methods will continue to be employed. The
17 Southern Ocean presents an additional challenge because of the importance
18 of mesoscale eddy fluxes, which occur on relatively small spatial and temporal
19 scales (Marshall and Speer, 2012).

20 A common approach in the Southern Ocean has been to infer distinct
21 components of the MOC in different ways. For instance, Sallée et al. (2010)
22 recently used ARGO data to estimate the steady geostrophic flow, satellite
23 data to calculate the Ekman pumping, and the eddy parameterization of
24 Gent and McWilliams (1990) to estimate the eddy-induced advection. The
25 divergence of these three components of the transport across the base of the
26 mixed layer then gives the net subduction and upwelling, i.e. the residual
27 MOC. A similar analysis of hydrographic data was performed by Speer et al.
28 (2000). One large uncertainty in this approach lies in the Gent-McWilliams
29 parameterization, which requires the specification of an eddy-transfer coeffi-
30 cient. Setting this eddy-transfer coefficient also presents a major uncertainty
31 in coarse-resolution numerical models.

32 Motivated by the importance of the eddy-driven component of the MOC,
33 much recent research has focused on characterizing the mixing properties of
34 mesoscale eddies in the Southern Ocean (Marshall et al., 2006; Sallée et al.,
35 2008; Smith and Marshall, 2009; Shuckburgh et al., 2009a,b; Abernathey
36 et al., 2010; Naveira-Garabato et al., 2011; Ferrari and Nikurashin, 2010; Lu
37 and Speer, 2010; Klocker et al., 2012a,b; Liu et al., 2012). A field campaign
38 to measure mixing rates, the Diapycnal and Isopycnal Mixing Experiment
39 in the Southern Ocean (a.k.a. DIMEs; Gille et al., 2012), is also underway.
40 The isopycnal mixing rates from these studies will be particularly valuable if
41 they can lead to improved estimates of the eddy-induced component of the

42 MOC in the Southern Ocean. However, a wide range of mixing diagnostics
43 have been employed, and the link between such diagnostics of mixing and
44 the actual eddy-induced transport is somewhat obscure. Furthermore, the
45 mixing rates measured by these studies are not necessarily the same as the
46 Gent-McWilliams eddy transfer coefficient (Smith and Marshall, 2009).

47 The goal of this paper is to directly compare various methods of diagnos-
48 ing lateral mixing. Some of these diagnostics are possible only in the context
49 of a numerical model, in which all the dynamical fields are known exactly.
50 We call these “perfect” diagnostics. We also consider less precise diagnostics
51 which can potentially be applied to the real ocean, for example, in DIMES.
52 We call these “practical” diagnostics.

53 This study builds on many previous works, beginning with Plumb and
54 Mahlman (1987), who first proposed the method for inferring \mathbf{K} , the eddy
55 diffusivity tensor, in an atmospheric model. A comparison between the diffu-
56 sivities of passive tracers, potential vorticity, and buoyancy was performed by
57 Treguier (1999) in a primitive-equation model and later in a quasi-geostrophic
58 model by Smith and Marshall (2009). Our study builds on their approach
59 by using primitive equations, including a more realistic residual meridional
60 overturning circulation, and by calculating diffusivities as functions of y and
61 z , rather than z alone. Marshall et al. (2006), Abernathey et al. (2010), Fer-
62 rari and Nikurashin (2010), and Lu and Speer (2010) all calculated “effective
63 diffusivity” based on the method of Nakamura (1996), but did not compare
64 their calculations to other mixing diagnostics. Klocker et al. (2012a) demon-
65 strated the equivalence between tracer and particle-based diffusivities, but
66 did so only in a 2D flow; here we work in three dimensions. In summary,
67 the program of this paper is to synthesize and summarize these disparate
68 methods in a flow with a plausible meridional overturning circulation, and
69 then to compare them with the less precise methods available in the field.

70 Our central conclusion is that disparate methods do in fact give reason-
71 ably similar results; we find roughly the same diffusivities for passive tracers,
72 Lagrangian floats, quasigeostrophic potential vorticity, and Ertel potential
73 vorticity. These all have similar magnitudes and vertical structures, with a
74 pronounced mid-depth maximum. But, as previously reported by Treguier
75 (1999) and Smith and Marshall (2009), none of them is similar to the Gent-
76 McWilliams coefficient, which has a lower magnitude and weak vertical struc-
77 ture.

78 **2. Numerical Model**

79 The model flow is meant to resemble the Antarctic Circumpolar Current.
80 The domain, numerical configuration, and forcing are identical to the model
81 described in Abernathey et al. (2011) and Hill et al. (2012), which the reader
82 should consult for a detailed description.

83 The Boussinesq primitive equations are solved using the MITgcm (Mar-
84 shall et al., 1997a,b). The domain is a zonally reentrant channel on a β -plane,
85 1000 km x 2000 km x 2985 m, forced at the surface with a wind stress and
86 a heat flux. The forcing and domain, along with a snapshot of the temper-
87 ature field, are illustrated in Fig. 1. There is a sponge layer at the northern
88 boundary, in which the temperature is relaxed to an exponential stratification
89 profile. A second-order-moment advection scheme is used to minimize spu-
90 rious numerical diffusion (Prather, 1986), resulting in an effective diapycnal
91 diffusivity of approx. $10^{-5} \text{ m}^2 \text{ s}^{-1}$ (Hill et al., 2012). The model contains no
92 salt and uses a linear equation of state, meaning that temperature, [negative]
93 density, and buoyancy are all equivalent.

94 The fine resolution (5 km in the horizontal, 40 vertical levels), together
95 with the forcing, which maintains a baroclinically unstable background state,
96 allows an energetic mesoscale eddy field to develop. Without the the sponge
97 layer, the eddy-induced overturning circulation would completely cancel the
98 wind-induced Eulerian-mean Ekman overturning circulation, resulting in zero
99 residual overturning circulation, a situation described by Kuo et al. (2005).
100 However, the presence of the sponge layer, in conjunction with the applied
101 pattern of heating and cooling, produces a residual overturning that qual-
102 itatively resembles the real Southern Ocean, as described by Marshall and
103 Radko (2003) or Lumpkin and Speer (2007) (see Abernathey et al., 2011, for
104 further detail).

105 This best measure of the residual overturning circulation is obtained by
106 averaging the meridional transport v in layers of constant buoyancy b ; the
107 streamfunction obtained this way is defined as

$$\Psi_{iso}(y, b) = \frac{1}{\Delta t} \int_{t_0}^{t_0 + \Delta t} \int \int_0^b (vh) db' dx dt , \quad (1)$$

108 where $h = -\partial z / \partial b$ is the layer thickness and b' is a dummy variable of
109 integration. In Fig. 2 we plot Ψ_{iso} in its native buoyancy coordinates and also
110 mapped back into depth coordinates. The figure reveals two distinct cells:
111 a clockwise lower cell, analogous to the Antarctic-Bottom-Water branch of

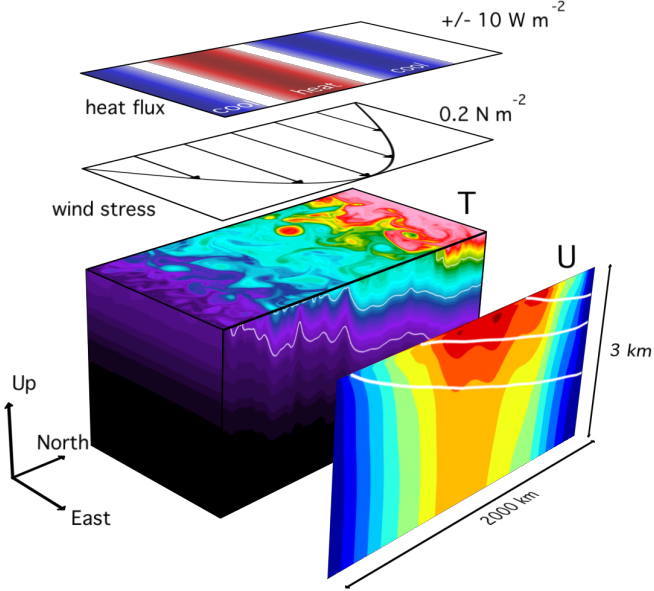


Figure 1: Overview of the model forcing and snapshot of temperature field. The colored box is the instantaneous temperature, ranging from 0 to 8°C. Above are the surface wind stress and heat flux fields. To the right is the time- and zonal-mean zonal velocity, contoured every 2.5 cm s^{-1} . *[[How do we get permission to use this from Abernathey et al. (2011)?]]*

the global MOC (Ito and Marshall, 2008); and a counterclockwise mid-depth cell, analogous to the upper branch of the global MOC (Marshall and Speer, 2012). There is also a shallow subduction region in the north of the domain that can be viewed as a mode-water formation region.

The fact that our model has non-zero interior residual circulation also implies that there are non-zero gradients and eddy fluxes of potential vorticity (PV) in the interior. These PV fluxes are directly related to the residual transport (Andrews et al., 1987; Plumb and Ferrari, 2005). The presence on non-zero interior PV is a key property that allows us to demonstrate the similarity in the mixing of dynamically passive tracers and floats to the dynamically active mixing of PV.

In the following sections, the velocity field from the equilibrated model will be used to advect passive tracers and particles.

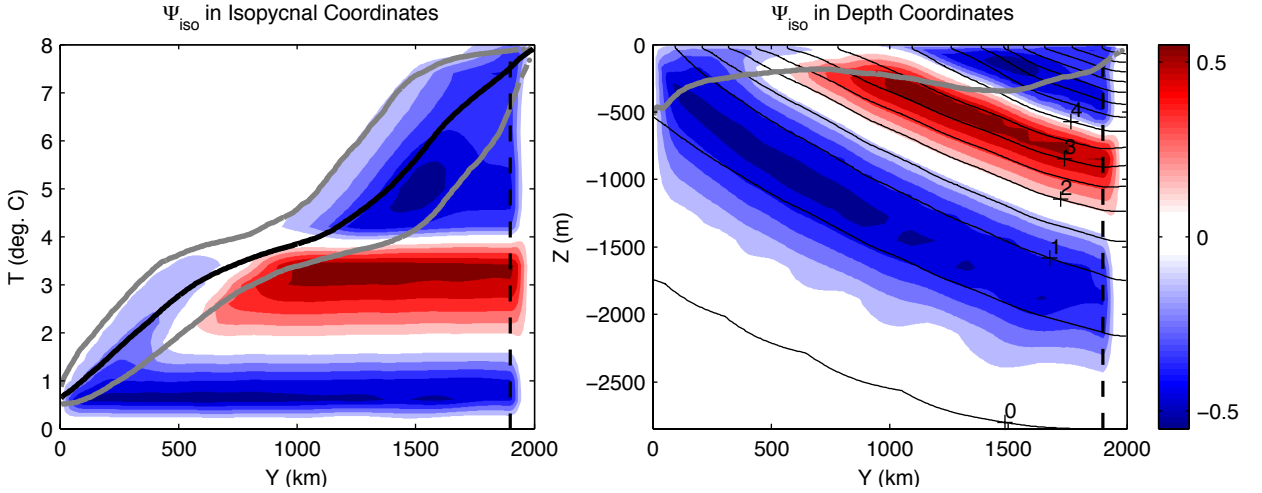


Figure 2: The residual overturning streamfunction in Sv (red for positive, blue for negative), calculated according to (1) in buoyancy coordinates (left) and depth coordinates (right). In the left panel, the gray contours delineate the upper and lower boundaries of the surface diabatic layer, and the black contour the mean sea-surface temperature. In the right panel, the black contours are the mean isopycnals and the gray contour is the bottom of the surface diabatic layer. *[[How do we get permission to use this from Abernathey et al. (2011)?]]*

125 3. Perfect Mixing Diagnostics

126 The *perfect* mixing diagnostics are quantities which can be calculated
 127 only with very detailed synoptic observation of the flow. Such diagnostics
 128 provide the most complete characterization of mixing and transport possible.
 129 They are straightforward to extract from numerical models but nearly im-
 130 possible for the real ocean. (By contrast, in the atmosphere, where detailed
 131 observations and reanalysis products provide sufficient spatial and tempo-
 132 ral resolution, many perfect diagnostics can be calculated (e.g. Haynes and
 133 Shuckburgh, 2000a,b).)

134 Observational problems aside, the interpretation of perfect mixing diag-
 135 nostics still poses a challenge. Different diagnostics have been used through-
 136 out the literature to characterize eddy mixing, and the relationship between
 137 these diagnostics is not always obvious. Our purpose here is to consolidate
 138 many different diagnostics in one place and show their relationship. A similar
 139 study was made for the atmosphere by Plumb and Mahlman (1987, hereafter
 140 PM87), who also review some theoretical aspects. Here we basically repeat

141 their methodology for this ACC-like flow.

142 *3.1. Passive Tracers*

143 Our starting point is to examine the mixing of passive tracers. Passive
144 tracers obey an advection-diffusion equation of the form

$$\frac{\partial c}{\partial t} + \mathbf{v} \cdot \nabla c = \kappa \nabla^2 c + C \quad (2)$$

145 where c is the tracer concentration, \mathbf{v} is the velocity field, κ is a small-scale
146 diffusivity, and C is a source or sink. We will focus on cases where $C = 0$ and
147 the diffusive term is negligible for the large-scale budget of c . (Some small-
148 scale diffusion is necessary for mixing to occur, and likewise it is impossible to
149 eliminate diffusion completely from numerical models. But for flows of large
150 Peclét number, diffusion is an important term only in the tracer *variance*
151 budget, not the tracer budget itself.)

152 *3.1.1. Diffusivity Tensor*

153 PM87 performed a detailed study of the transport characteristics of a
154 model atmosphere using passive tracers. Here we briefly review their def-
155inition of \mathbf{K} , the diffusivity tensor, which we view as the most complete
156 diagnostic of eddy-transport. The reader is referred to PM87 for a more
157 in-depth discussion.

158 Taking a zonal average of (2) (indicated by an overbar) and neglecting
159 the RHS terms, we obtain

$$\frac{\partial \bar{c}}{\partial t} + \bar{\mathbf{v}} \cdot \nabla \bar{c} = -\nabla \cdot \mathbf{F}_c \quad (3)$$

160 where $\mathbf{F}_c = (\overline{v'c'}, \overline{w'c'})$ is the eddy flux of tracer in the meridional plane.
161 The diffusivity tensor \mathbf{K} relates this flux to the background gradient in each
162 direction; it is defined by

$$\mathbf{F}_c = -\mathbf{K} \cdot \nabla \bar{c} . \quad (4)$$

163 This equation is underdetermined for a single tracer, but PM87 used multiple
164 tracers with different background gradients to calculate it. This method has
165 also recently been applied by Fox-Kemper et al. (2012) in an oceanic context.

166 We found \mathbf{K} by solving (4) for six independent tracers. In this case,
167 (4) is overdetermined, and the “solution” is a least-squares best fit (Fox-
168 Kemper et al., 2012). The initial tracer concentrations used were as follows:

169 $c_1 = y$, $c_2 = z$, $c_3 = \cos(\pi y/L_y) \cos(\pi z/H)$, $c_5 = \sin(\pi y/L_y) \sin(\pi z/H)$,
 170 $c_5 = \sin(\pi y/L_y) \sin(2\pi z/H)$, $c_6 = \cos(2\pi y/L_y) \cos(\pi z/H)$. (We exper-
 171 imented with different initial concentrations, but found the results to be in-
 172 sensitive to this detail, provided many tracers with different gradients were
 173 used.) The tracers were allowed to evolve from these initial conditions for
 174 one year. (An experiment with two years of evolution produced very similar
 175 results.) \mathbf{F}_c and $\nabla \bar{c}$ were calculated for each tracer by performing a zonal
 176 and time average over the one-year period and then over an ensemble of 20
 177 different years. In matrix form, the equation solved to find $\mathbf{K}(y, z)$ was

$$\begin{bmatrix} \overline{v'c'_1} & \overline{v'c'_2} & \dots & \overline{v'c'_6} \\ \overline{w'c'_1} & \overline{w'c'_2} & \dots & \overline{w'c'_6} \end{bmatrix} = - \begin{bmatrix} K_{yy} & K_{yz} \\ K_{zy} & K_{zz} \end{bmatrix} \begin{bmatrix} \partial \bar{c}_1 / \partial y & \partial \bar{c}_2 / \partial y & \dots & \partial \bar{c}_6 / \partial y \\ \partial \bar{c}_1 / \partial z & \partial \bar{c}_2 / \partial z & \dots & \partial \bar{c}_6 / \partial z \end{bmatrix} \quad (5)$$

178 where each element of \mathbf{K} at each point in (y, z) space is a least-squares esti-
 179 mate that minimizes the error across all tracers.

180 It is most informative to decompose \mathbf{K} into two parts,

$$\mathbf{K} = \mathbf{L} + \mathbf{D} , \quad (6)$$

181 where \mathbf{L} is an antisymmetric tensor and \mathbf{D} is symmetric. Because the flux due
 182 to \mathbf{L} is normal to $\nabla \bar{c}$, its effects are advective, rather than diffusive (Plumb,
 183 1979; Plumb and Mahlman, 1987; Griffies, 1998). Using this fact, we can
 184 rewrite (3) as

$$\frac{\partial \bar{c}}{\partial t} + (\bar{\mathbf{v}} + \mathbf{v}^\dagger) \cdot \nabla \bar{c} = \nabla \cdot (\mathbf{D} \cdot \nabla \bar{c}) \quad (7)$$

185 where $\mathbf{v}^\dagger = (v^\dagger, w^\dagger)$ is an eddy-induced effective transport velocity, defined
 186 by a streamfunction χ , such that

$$v^\dagger = -\partial \chi / \partial z , \quad w^\dagger = \partial \chi / \partial y \quad (8)$$

187 and

$$\mathbf{L} = \begin{bmatrix} 0 & -\chi \\ \chi & 0 \end{bmatrix} . \quad (9)$$

188 Under adiabatic conditions, χ is approximatey equal to the transformed-
 189 Eulerian-mean eddy-induced streamfunction, or the “bolus transport” stream-
 190 function in thickness-weighted isopycnal coordinates. Again, for more de-
 191 tailed discussion, the reader is referred to PM87.

192 Because \mathbf{L} is advective in nature (and doesn’t appear in the tracer variance
 193 budget), all of the actual *mixing* due to eddies in contained in \mathbf{D} (Nakamura,

194 2001). Since \mathbf{D} is symmetric, it can be diagonalized by rotation through an
195 angle α where

$$\tan 2\alpha = \frac{2D_{yz}}{D_{yy} - D_{zz}}. \quad (10)$$

196 The rotated matrix,

$$\mathbf{D}' = \begin{bmatrix} D'_{yy} & 0 \\ 0 & D'_{zz} \end{bmatrix} = \begin{bmatrix} \cos \alpha & -\sin \alpha \\ \sin \alpha & \cos \alpha \end{bmatrix} \mathbf{D} \quad (11)$$

197 describes the eddy diffusion along (D'_{yy} , the *major-axis* diffusivity) and across
198 (D'_{zz} , the *minor-axis* diffusivity) the plane defined by α , which we call the
199 *mixing angle*.

200 The physical interpretation of \mathbf{K} is therefore best summarized by four
201 quantities: χ , α , D'_{yy} , and D'_{zz} . These quantities are plotted in Fig. 3. The
202 mixing angle is along isopycnals throughout most of the domain, except close
203 to the surface, where the mixing acquires a more horizontal character. This
204 pattern is consistent with the paradigm that ocean eddies mix adiabatically
205 in the interior and diabatically in the “surface diabatic layer,” i.e. the layer
206 over which isopycnals outcrop (Treguier et al., 1997; Cerovecki and Marshall,
207 2008). Consequently, D'_{yy} can be described as an *isopycnal* eddy diffusivity,
208 and D'_{zz} as *diapycnal* eddy diffusivity.

209 An obvious feature in the spatial structure of D'_{yy} is a pronounced peak at
210 mid-depth (approx. 1200 m). Enhanced lateral mixing at a mid-depth “crit-
211 ical layer” is a general feature of baroclinically unstable jets (Green, 1970;
212 Killworth, 1997). Many studies have confirmed the presence of an enhanced
213 mid-depth mixing layer in the ACC (Smith and Marshall, 2009; Abernathey
214 et al., 2010; Naveira-Garabato et al., 2011; Klocker et al., 2012a). Our highly
215 idealized model evidently shares this behavior. It is also important to note,
216 though, that D'_{yy} varies even more strongly with y , with the strongest mixing
217 being in the center of the channel.

218 The interpretation of D'_{zz} is more puzzling. The major-axis diffusivity
219 is much greater than the minor: $|D'_{yy}|/|D'_{zz}| \simeq 10^7$. Combined with the
220 fact that α departs only very slightly from 0 (due to the aspect ratio of the
221 domain), this means that $D'_{yy} \simeq D_{yy}$. On the other hand, each individual
222 component of \mathbf{D} is much greater in magnitude than D'_{yy} , whose value de-
223 pends on large cancellations in (11). The implied diapycnal diffusivity of
224 $O(10^{-4}) \text{ m}^2 \text{ s}^{-1}$ is at odds with a previous study focused exclusively on di-
225 apycnal mixing (Hill et al., 2012), which found values of $O(10^{-5}) \text{ m}^2 \text{ s}^{-1}$ and

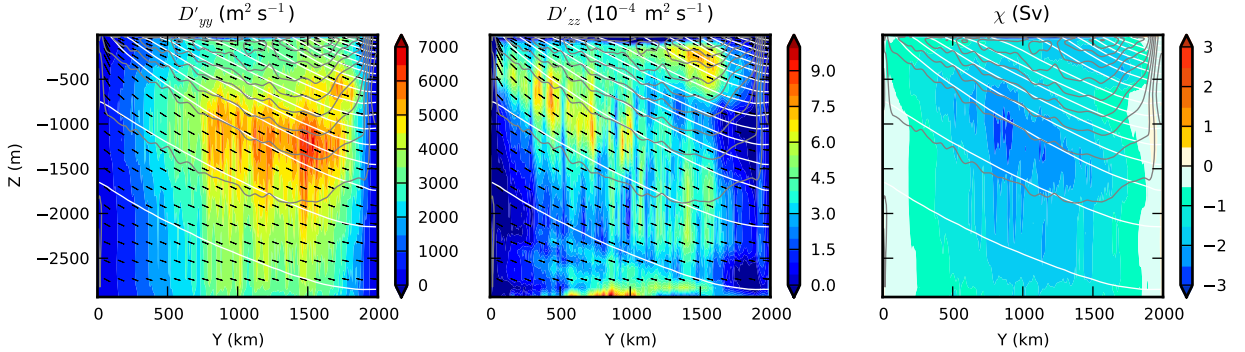


Figure 3: Decomposition of eddy diffusivity tensor \mathbf{K} into a major-axis diffusivity D'_{yy} , minor-axis diffusivity D'_{zz} , and eddy-induced transport stream function χ . χ has been converted to Sv by multiplying by L_x . The mean isopycnals are shown in white contours (contour interval 0.5°C), and the thermal-wind component of the zonal-mean velocity is shown in grey (contour interval 1 cm s^{-1}). In the left two panels, the mixing angle α is indicated by the black dashes. See text for discussion.

226 below in the same model using different methods. Our conclusion is that
 227 even a very small error in α can cause D'_{zz} to be polluted with spurious large
 228 values, and that the multiple-tracer method described here is not a robust
 229 diagnostic of diapycnal mixing. The focus of the present study is on lateral
 230 mixing, and we will not concern ourselves with D'_{zz} further here.

231 The eddy transport streamfunction χ , shown in the third panel of Fig. 3,
 232 describes a counterclockwise overturning circulation that opposes the Ekman
 233 circulation. It has the same magnitude and structure as the eddy-induced
 234 overturning computed using thickness-weighted isopycnal averaging, as de-
 235 scribed in detail in Abernathey et al. (2011).

236 3.1.2. Nakamura Effective Diffusivity

237 The framework developed by Nakamura (1996) has gained widespread use
 238 in assessing lateral mixing in the ocean and atmosphere (Nakamura and Ma,
 239 1997; Haynes and Shuckburgh, 2000a,b; Marshall et al., 2006; Abernathey
 240 et al., 2010; Klocker et al., 2012a). This framework relies on a tracer-based
 241 coordinate system, in which the flux across tracer isosurfaces can be charac-
 242 terized by an effective diffusivity, which depends only on the instantaneous
 243 tracer geometry. A similar concept was developed by Winters and D’Asaro
 244 (1996).

245 The effective diffusivity is defined as

$$K_{eff} = \kappa \frac{L_e^2}{L_{min}^2} \quad (12)$$

246 where L_e is the equivalent length of a tracer contour that has been stretched
247 by eddy stirring and L_{min} is the minimum possible length of such a contour,
248 in this case, simply the domain width in the zonal direction. For further
249 background and details regarding the K_{eff} calculation, the reader is referred
250 to Marshall et al. (2006).

251 As described in the preceding section, the model was constructed to be
252 as adiabatic as possible, with explicit horizontal and vertical diffusion set to
253 zero. However, the effective diffusivity framework requires a constant small-
254 scale background horizontal diffusivity κ . Therefore, in the tracer advection
255 for the effective diffusivity experiments, we used an explicit horizontal diffu-
256 sivity of $\kappa = 50 \text{ m}^2 \text{ s}^{-1}$. Analysis of the tracer variance budget indicated that
257 numerical diffusion elevated this value slightly, to $55 \text{ m}^2 \text{ s}^{-1}$. We performed
258 our experiments by initializing a passive tracer with concentration $c = y$
259 and allowing it to evolve under advection and diffusion for two years. Every
260 month, a snapshot of c and T was output. This procedure was repeated for
261 10 consecutive two-year periods, to create a smooth ensemble-average picture
262 of the evolution of K_{eff} over two years.

263 The 3D tracer field must be sliced into 2D surfaces in order to compute
264 $K_{eff}(y)$. The most straightforward way to accomplish this is to examine
265 surfaces of c at constant z ; we call this K_{eff}^H . However, since the mixing
266 angle is along isopycnals, a more physically relevant choice is to project c into
267 isopycnal coordinates; the effective diffusivity computed from this projection
268 we call K_{eff}^{iso} . Abernathey et al. (2010) tried both methods, and here we do
269 the same.

270 After two months, the overall magnitude of both K_{eff} calculations sta-
271 bilizes and remains roughly constant, as does the spatial structure of K_{eff}^{iso} .
272 The spatial structure of K_{eff}^H , on the other hand, continues to evolve over the
273 two year period, departing further and further from K_{eff}^{iso} . The results of one
274 K_{eff} ensemble calculation (at 10 months) are shown in Fig. 4. Comparing
275 this figure with Fig. 3, we see that K_{eff}^{iso} is strikingly similar in magnitude
276 and spatial structure to D'_{yy} . This agreement between these two diagnostics,
277 based on quite different methods, is expected but nevertheless encouraging.
278 K_{eff}^H , on the other hand, while having the right general magnitude, has sig-
279 nificant differences in spatial structure. From this we conclude that K_{eff}^H

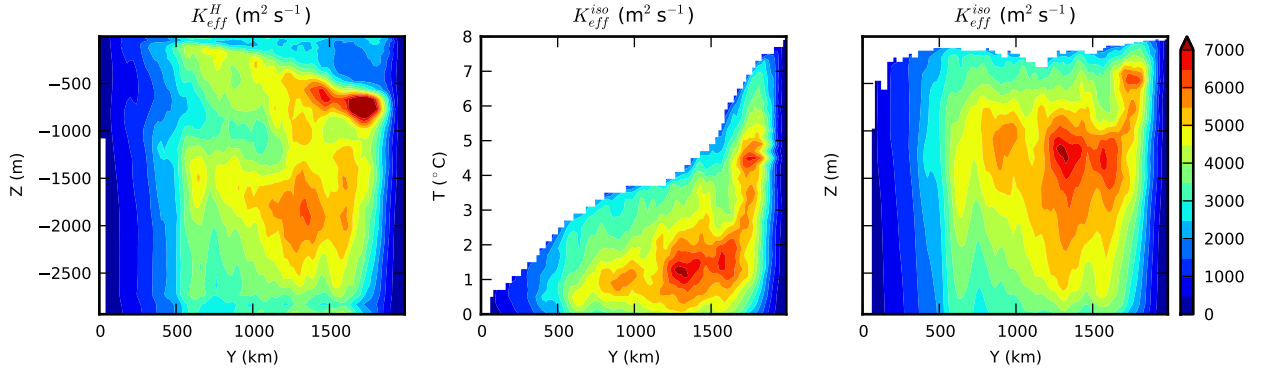


Figure 4: Nakamura effective diffusivity calculated on a passive tracer after 10 months of evolution. Values shown are an average over an ensemble of 10 independent tracer-release experiments. In the left panel, K_{eff}^H was calculated on slices of c at constant z (horizontal). In the middle panel, K_{eff}^{iso} was calculated on slices of c at constant T (isopycnal). The right panel shows K_{eff}^{iso} mapped back to depth space using the mean isopycnal depths.

280 is somewhat misleading diagnostic whose physical interpretation is unclear.
 281 K_{eff}^{iso} , on the other hand, is a robust diagnostic of isopycnal mixing.

282 3.2. Active Tracers

283 Here we compute flux-gradient diffusivities for active tracers. By active
 284 tracers we mean scalars which obey (2) but which also affect the dynamics of
 285 the flow. The active tracers we consider are potential vorticity and buoyancy.
 286 Also, unlike the passive tracers, these active tracers are forced at the surface,
 287 and their zonal means have reached a steady-state equilibrium. Therefore,
 288 it is interesting to ask whether they experience the same diffusivity as the
 289 passive tracers.

290 3.2.1. QGPV Diffusivity

291 Quasi-geostrophic theory predicts that stirring by mesoscale eddies will
 292 lead to a down-gradient flux of quasi-geostrophic potential vorticity (QGPV)
 293 in the ocean interior (Rhines and Young, 1982). Although this down-gradient
 294 relationship cannot be expected to hold locally at every point in the ocean,
 295 it is much more robust in a zonally-averaged context, which eliminates rotat-
 296 tional fluxes from the enstrophy budget (Marshall and Shutts, 1981; Wilson
 297 and Williams, 2004). Although our model is based on primitive equations,

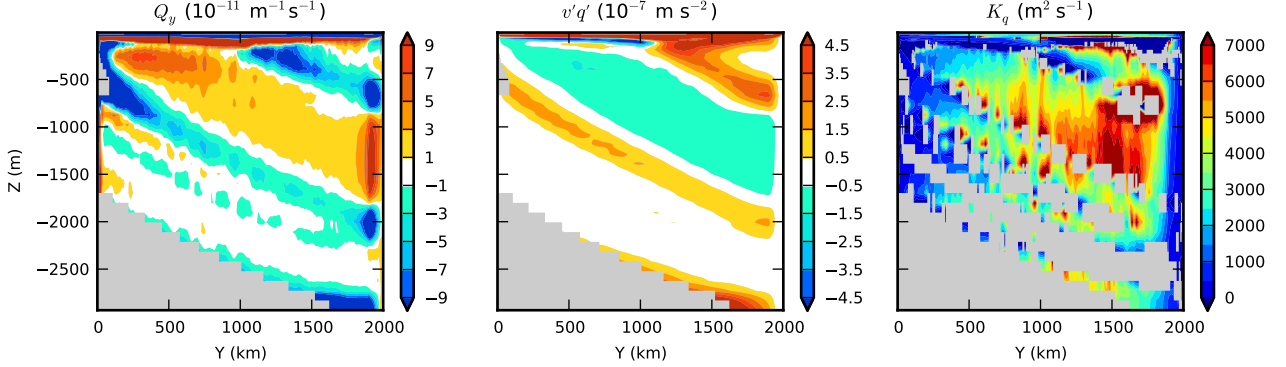


Figure 5: Left panel: mean meridional QGPV gradient Q_y . Middle: eddy qgpv flux $\overline{v'q'}$. Right: qgpv diffusivity K_q . The left two quantities were masked where $\bar{b}_z < 2 \times 10^{-7} \text{ s}^{-1}$ (i.e. weak stratification) to avoid dividing by this small number. K_q was additionally masked in places where $|Q_y| < \beta/2$, where the QGPV gradient crosses zero. The masked areas are colored gray.

298 certain quasi-geostrophic quantities can nevertheless be calculated (Treguier
299 et al., 1997). Of interest here is the eddy QGPV flux ¹

$$\overline{v'q'} = f_0 \frac{\partial}{\partial z} \left(\frac{\overline{v'b'}}{\bar{b}_z} \right) \quad (13)$$

300 and the background meridional QGPV gradient

$$Q_y = \beta - f_0 \frac{\partial s_b}{\partial z} . \quad (14)$$

301 The QGPV diffusivity is then defined as

$$K_q = -\overline{v'q'}/Q_y . \quad (15)$$

302 All three of these quantities are plotted in Fig. 5. First we note that,
303 where Q_y is nonzero, there is indeed a strong anti-correlation between Q_y
304 and $\overline{v'q'}$, supporting the notion of a down-gradient transfer of QGPV. This is

¹The QGPV flux also includes a Reynolds-stress term $\partial_y(\overline{u'v'})$. In our model, this term is an order of magnitude smaller, as expected from standard oceanographic scaling arguments (Vallis, 2006), and has therefore been neglected.

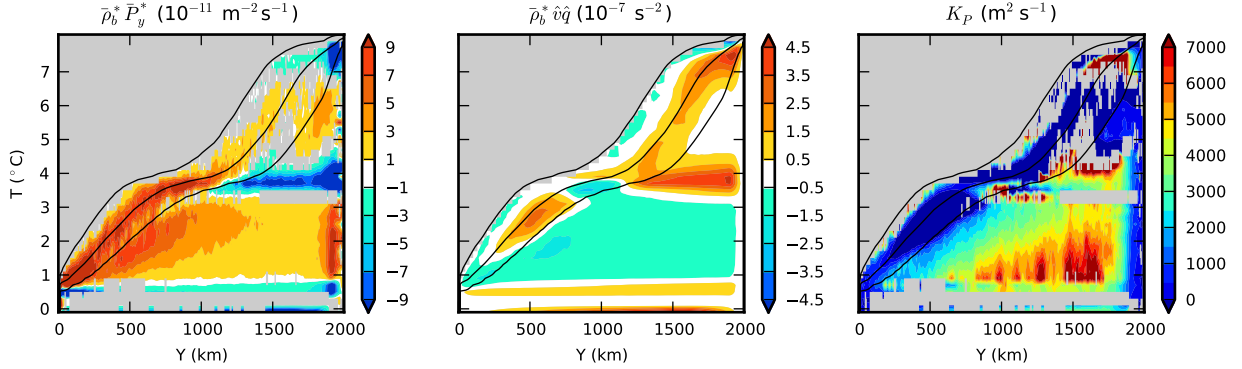


Figure 6: Left panel: mean meridonal / isopycnal Ertel PV $\bar{\rho}_b^* \bar{P}_y^*$, plotted in buoyancy space. (Multiplication by the factor $\bar{\rho}_b^*$ gives the same units as the QGPV gradient in Fig. 5.) See Appendix A for details. Middle: eddy Ertel PV flux $\bar{\rho}_b^* \hat{v} \hat{P}$. Right: Ertel PV diffusivity K_P . As in Fig. 5, the gradient has been masked where its absolute value is less than $\beta/2$. The masked areas are colored gray. The black contours indicate the 5%, 50%, and 95% levels of $\bar{\Pi}$.

305 reflected by the fact that K_q is positive nearly everywhere. (The relationship
 306 breaks down near the surface, which we attribute to the presence of strong
 307 forcing terms and an unstratified mixed layer, making the QG approximation
 308 itself invalid.) Furthermore, comparing Fig. 5 with Fig. 3, we see a strong
 309 resemblance between K_q and D'_{yy} , both in magnitude and spatial structure.
 310 The calculation of K_q involves computing many derivatives in both y and
 311 z . We expected to find a very noisy result, and are consequently pleasantly
 312 surprised by this agreement. K_q is also very similar to K_{eff}^{iso} , supporting the
 313 choice by Abernathey et al. (2010) to equate these quantities in a diffusive
 314 closure for the eddy QGPV flux.

315 3.2.2. Isopycnal Ertel PV Diffusivity

316 Through the well-known correspondence between the quasigeostrophic
 317 framework and analysis in isopycnal coordinates, the QGPV flux can be
 318 recast as a flux of Ertel potential vorticity along isopycnals (Andrews et al.,
 319 1987). Analysis of the tracer variance budget in isopycnal coordinates also
 320 supports a down-gradient diffusive closure for the PV flux in this framework
 321 (Jansen and Ferrari, 2012). Here we calculate the along-isopycnal Ertel PV
 322 diffusivity directly.

323 The isopycnal diffusivity of Ertel potential vorticity is defined as

$$K_P = -\bar{v}\hat{P}^*/\frac{\partial \bar{P}^*}{\partial y} \quad (16)$$

324 where P is the Ertel potential voricity. The details of the notation and
325 the thickness-weighted averaging in isopycnal coordinates are described in
326 Appendix A. All the factors in (16) are plotted in Fig. 6, in buoyancy space
327 rather than depth. The strong similarity between the fluxes and gradients in
328 the QG and isopycnal frameworks confirms the mathematical correspondence
329 between these two forms of analysis. Furthermore, the spatial structure and
330 magnitude of K_P in the interior is quite similar to K_{eff}^{iso} and, when mapped
331 back to depth coordinates (not plotted), to D'_{yy} and K_q .

332 *3.2.3. Buoyancy Diffusivity*

333 The horizontal buoyancy diffusivity is an important yet problematic quan-
334 tity, defined as

$$K_b = -\frac{\bar{v}'\bar{b}'}{\bar{b}_y}. \quad (17)$$

335 This quantity plays a central role in eddy parameterization (Gent and McWilliams,
336 1990; Gent et al., 1995; Griffies, 1998) and in the theory of the Southern
337 Ocean overturning circulation (Marshall and Radko, 2003; Nikurashin and
338 Vallis, 2012). (It is commonly also referred to as the Gent-McWilliams eddy
339 transfer coefficient.) Yet it is not, properly speaking, a diffusivity in the
340 Fickian sense. This is because, in the adiabatic interior, the eddy buoy-
341 ancy flux \mathbf{F}_b (of which $\bar{v}'\bar{b}'$ is only one component) is directed almost entirely
342 *perpendicular* to the buoyancy gradient (Griffies, 1998; Plumb and Ferrari,
343 2005). There is no down-gradient eddy flux of buoyancy, only a “skew flux.”
344 Therefore, using (4) and (6), we see that

$$K_b \simeq \chi/s_b \quad (18)$$

345 where $s_b = -(\partial \bar{b}/\partial y)/(\partial \bar{b}/\partial z)$ is the mean isopycnal slope. (This relation is
346 in fact a key assumption of the Gent and McWilliams (1990) parameteriza-
347 tion.) The buoyancy diffusivity K_b is related to the eddy-induced stream-
348 function χ and the isopycnal slope.

349 We have plotted both sides of (18) in Fig. 7, illustrating the similarity
350 between the two quantities, as well as the significant differences between

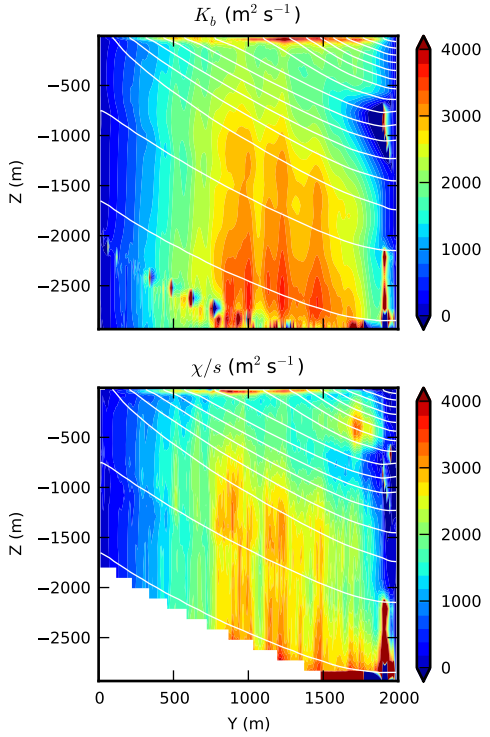


Figure 7: Left panel: horizontal buoyancy diffusivity K_b calculated from (17). Right panel: χ/s_b .

351 K_b and D'_{yy} . Noting the different color scales used in Figs. 7 and 3, it is
352 evident that overall magnitude of K_b is roughly half that of D'_{yy} . Significant
353 differences in spatial structure are also present. For instance, K_b has its
354 highest values at the bottom and top of the water column, while D'_{yy} has
355 its maximum at mid-depth. It is particularly important to point out these
356 differences because it is quite common to assume that $D'_{yy} = K_b$ in the
357 context of eddy parameterization (Gent and McWilliams, 1990; Gent et al.,
358 1995; Griffies, 1998). Such an assumption is clearly not supported by our
359 simulations. Similarly, Liu et al. (2012) used an adjoint-based method to
360 infer K_b and then discussed the results in terms of the mixing-length ideas
361 of Ferrari and Nikurashin (2010). Our results suggest this comparison is
362 unsound. In Sec. 5, we will further explore the relationship between K_b and
363 D'_{yy} and discuss the parameterization problem.

364 *3.3. Summary*

365 So far in this section we have seen strong agreement between different
366 perfect diagnostics of isopycnal mixing. In particular, D'_{yy} , K_{eff}^{iso} , K_q , and
367 K_P all give a similar picture of along-isopycnal mixing rates. The strength of
368 along-isopycnal mixing varies between 3000 and 7000 $\text{m}^2 \text{s}^{-1}$ in the middle
369 of the domain, with a pronounced peak between 1000 and 1500 m depth.
370 Mixing rates fall off sharply at the northern and southern edges of the domain.
371 However, the buoyancy diffusivity K_b does not agree with the other mixing
372 diagnostics, differing both in magnitude and vertical structure. This result
373 has been found by previous authors (Treguier, 1999, SM09) and results from
374 the fact that K_b is a “skew” diffusivity rather than an isopycnal diffusivity
375 (Griffies, 1998). We now turn to the question of how, and how accurately,
376 the isopycnal mixing rates can be inferred from experiments in the field.

377 **4. Practical Mixing Diagnostics**

378 *4.1. Lagrangian Diffusivity*

379 One of the two most common methods to estimate isopycnal diffusion in
380 observational programs is the use of Lagrangian trajectories of either surface
381 drifters or subsurface floats (e.g. Davis, 1991; LaCasce, 2008). (The other
382 method, described in the next subsection, is to use tracer release experi-
383 ments.) Lagrangian diffusivities are calculated from the mean square separa-
384 tion of drifters and floats (called simply “particles” from here on) from their
385 starting positions. This is the single-particle diffusivity of Taylor (1921):

$$K_{1y}(y_0, t) = \frac{1}{2} \frac{d}{dt} \langle (y(t) - y_0)^2 \rangle . \quad (19)$$

386 Here $y(t)$ is the meridional position of a particle released at y_0 at $t = 0$
387 and $\langle \cdot \rangle$ is the average over all particles. Lagrangian diffusivities can also
388 be calculated using the mean-square separation of particles relative to each
389 other. This is the relative (or two-particle) diffusivity:

$$K_{2y}(y_0, \Delta r_0, t) = \frac{1}{4} \frac{d}{dt} \langle (y_i(t) - y_j(t))^2 \rangle . \quad (20)$$

390 Here $y_i(t)$ and $y_j(t)$ are the meridional positions of particles i and j released
391 within a distance Δr_0 of each other (y_0 is the initial condition of either the
392 i or j particle); the ensemble average is taken over many such pairs. Both

393 the single-particle diffusivity and the relative diffusivity asymptote at long
 394 times (e.g. Davis, 1985). As shown by Taylor (1921), these eddy diffusivities
 395 are equal to the integral of the Lagrangian autocorrelation function, which
 396 in case of the single-particle diffusivity can be written as:

$$K_{1y}(y_0, t) = \int_0^t R_{vv}(y_0, \tau) d\tau \quad \text{where} \quad R_{vv}(y_0, \tau) = \langle v_L(y_0, \tau) v_L(y_0, 0) \rangle. \quad (21)$$

397 Here v_L is the Lagrangian velocity of the particle. If the Lagrangian velocities
 398 decorrelate after a certain time, and the integral of the correlation is finite.
 399 The Lagrangian diffusivity $K_{1y}(y_0, t)$ will consequently asymptote to a con-
 400 stant value (Taylor, 1921), which then results in eddy diffusivities equivalent
 401 to those estimated using tracer-based estimates, as shown by Klocker et al.
 402 (2012b).

403 Here it is important to note that it is necessary to have sufficient La-
 404 grangian statistics to resolve this Lagrangian autocorrelation function until
 405 it decorrelates; the error is expected to decrease as $n^{-1/2}$, where n is the
 406 number of particles (Davis, 1994). Klocker et al. (2012b) have shown that
 407 this Lagrangian autocorrelation function has two parts—an exponential de-
 408 caying part and an oscillatory part. If integrating just over the exponential
 409 decaying part (as done in many observational studies in the past) one would
 410 derive an eddy diffusivity for the case in which the mean flow does not influ-
 411 ence the diffusivity. But as shown by several recent studies (Marshall et al.,
 412 2006; Abernathey et al., 2010; Ferrari and Nikurashin, 2010), eddy diffu-
 413 sivities are influenced by the mean flow; this can be seen as the oscillatory
 414 part of the Lagrangian autocorrelation function (Klocker et al., 2012b). Re-
 415 solving this oscillatory part requires a much larger number of particles, and
 416 therefore leads to strong limitations in observational programs due to the lim-
 417 ited number of drifters and floats deployed in those programs. (See Klocker
 418 et al. (2012b) for a more detailed exploration of the issue of using limited
 419 Lagrangian statistics to derive eddy diffusivities in observational studies.)

420 In numerical simulations, we can just increase the number of floats until
 421 the errors are sufficiently small. To calculate eddy diffusivities in this study,
 422 floats are deployed at every grid point (i.e. every 5 km) within a region
 423 which extends over the whole model domain in the zonal direction and over
 424 a width of 100 km, centered in the channel, in meridional direction. The
 425 floats are then advected for one year, with positions output every day. This
 426 float advection is repeated for every depth level of the model. Lagrangian

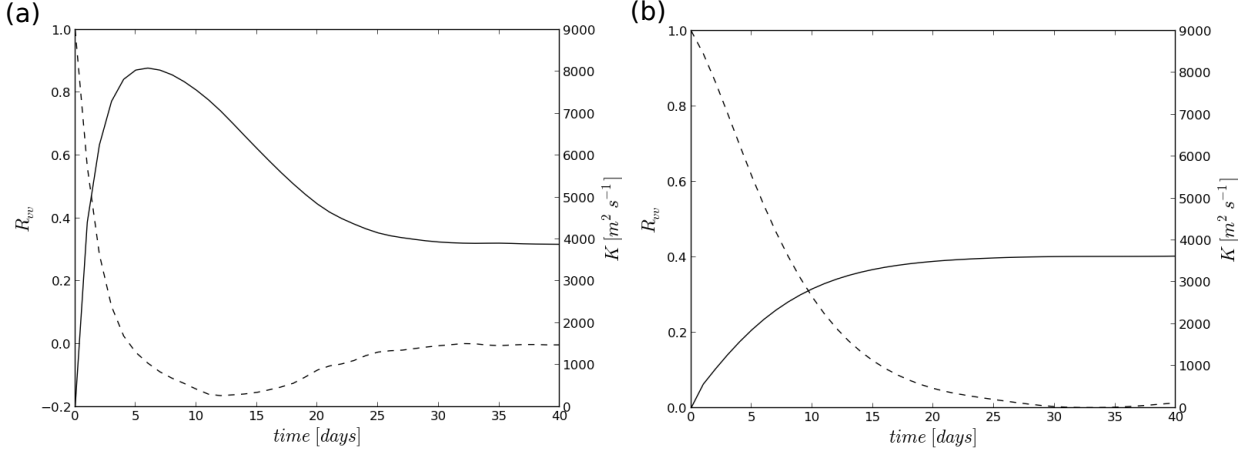


Figure 8: Lagrangian autocorrelation function R_{vv} (dashed) and K_{1y} (solid) from the particle release experiments at depths of (a) 100 m and (b) 1500 m.

eddy diffusivities are calculated according to (21), with the eddy diffusivity being calculated as an average over days 30-40. Examples for the Lagrangian autocorrelation function, R_{vv} , and the Lagrangian eddy diffusivity, K_{1y} are shown in Fig. 8a for floats deployed at a depth of 100 m and 8b for floats deployed at a depth of 1500 m. Fig. 8a shows a typical example for a depth where the mean flow plays an important role in suppressing eddy diffusivities, with R_{vv} showing an exponential decay and an oscillatory part, leading to an eddy diffusivity K_{1y} which first increases to approx. $8000 \text{ } m^2 s^{-1}$ and then converges at approx. $4000 \text{ } m^2 s^{-1}$. Fig. 8b shows both R_{vv} and K for a depth where the mean flow does not play an important role, i.e. R_{vv} only shows an exponential decay and K increases until converging at approx. $3700 \text{ } m^2 s^{-1}$. In both cases the Lagrangian autocorrelation function decorrelates after approx. 30 days. The vertical profile of Lagrangian diffusivities is shown in Fig. 12 (the overall comparison figure, discussed subsequently) and agrees well with other estimates of eddy diffusivities.

4.2. Tracer Release

Another possible method to measure isopycnal diffusion in the ocean is through the use of deliberate tracer release experiments. Such techniques have already been successfully employed to estimate diapycnal mixing by Ledwell and collaborators (Ledwell and Bratkovich, 1995; Ledwell et al.,

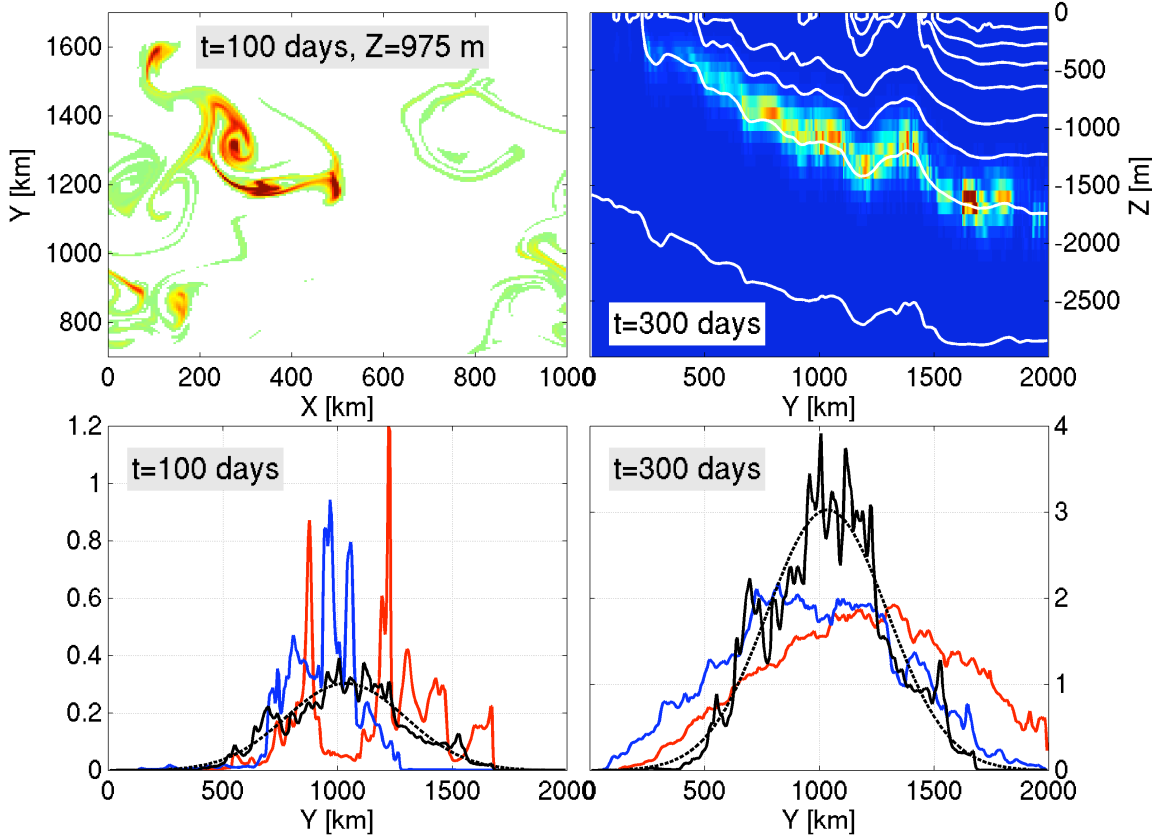


Figure 9: (top, left) Horizontal tracer distribution at 975 m depth, 100 days after release near $(x, y) = (500, 1000)$ km at 975 m depth. Note that only a subdomain is shown. Only tracer concentration larger than 10^{-5} are plotted. (top, right) Meridional section through the channel at $X = 1000$ km showing a snap-shot of the tracer distribution (color) and temperature surfaces (white contours) 300 days after release (same release as that show in top left panel). (bottom left) Meridional profiles of the vertically and zonally averaged tracer concentration (in 10^{-4} units) 100 days after release: the red and blue curves shows two examples of a single tracer release while the solid black surge shows the ensemble mean of all 16 tracer releases. The dashed black line is the least-squared fit Gaussian curve to the ensemble mean distribution. (bottom right) Same as bottom left but after 300 days (in 10^{-5} units).

1998, 2011). In these experiments, a passive dye is released as close as technically possible to a target isopycnal in the ocean and its subsequent evolution monitored over a few years. To quantify the vertical diffusion, the tracer field is first isopycnally averaged into one vertical profile. These profiles are well approximated by a Gaussian whose width σ evolves linearly with time (as expected if the tracer field spread vertically according to a simple one dimensional diffusion equation). The vertical diffusion κ_v is then given by $\kappa_v = (1/2)d\sigma/dt$. This method was also successfully applied to the estimation of the effective diapycnal diffusion in a numerical model in a setup very similar to the one used here (Hill et al., 2012).

One hopes that isopycnal diffusion in the ocean could be estimated using similar techniques by taking advantage of already collected data (e.g. from the NATRE and DIMES campaigns; Ledwell et al., 1998; Gille et al., 2012). To achieve this, one could monitor the isopycnal spreading of the tracer by summing its 3D distribution vertically. To simplify further the problem here, we will zonally average the resulting 2D map into a 1D profile and focus on the meridional diffusivity K_I . Unfortunately, one can readily see that the tracer distribution is very patchy and its meridional profile is poorly approximated by a Gaussian. Fig. 9 illustrates this point in the channel, plotting the tracer distribution 100 days after release. (Details of the experiments and diagnostic methods are given in Appendix B.) The tracer patch is stretched into long narrow filaments, cascading to small scales. Such behavior is also observed in the real ocean (see Fig. 18 from Ledwell et al., 1998). Unlike the diapycnal case, the isopycnal dispersion of a tracer patch does not fit a one-dimensional diffusion equation, at least initially, effectively preventing a reliable estimation of K_I .

One possible way to circumvent this issue is to consider an ensemble of tracer releases. One expects that in an average sense, the tracer does behave in a diffusive way. To test this, we perform 16 tracer releases in the model: 8 tracers are released simultaneously 125 km apart along the center of the channel, followed by a second set of 8 releases 300 days later. The ensemble-mean profiles at 100 and 300 days after release are shown in Fig. 9 (bottom, black solid). Contrary to profiles from single releases, the ensemble-mean profile already approaches a Gaussian shape after 100 days. Importantly, the width of the best-fit Gaussian curve to the ensemble-mean profile (dashed black) grows linearly with time after 150 days at most depths (see Appendix B for details).

The isopycnal diffusivity in the channel, estimated from the 16-member

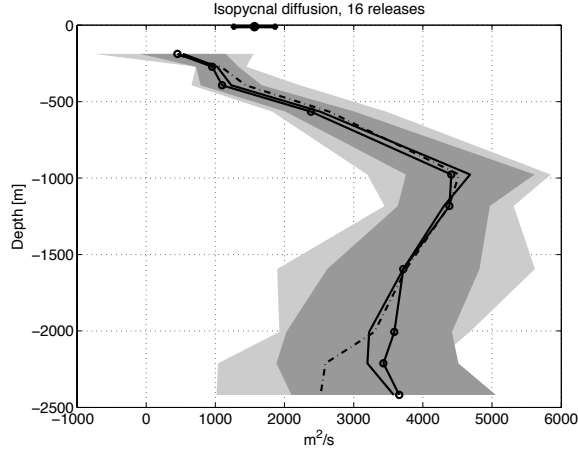


Figure 10: Vertical profiles of the isopycnal diffusivity K_I estimated from tracer release experiments in the channel. The thick line denotes values estimated from monitoring the evolution of the 16-member ensemble-mean tracer at each depth. The mean (\pm one standard deviation) of isopycnal diffusivities computed by following each tracer individually (16 values) are shown by a dashed-dotted line and light grey shading. Similar quantities from 2-member ensemble-mean are shown in solid black and dark grey shading.

485 ensemble mean, is plotted as a function of depth in Fig. 10. It increases
 486 from about $500 \text{ m}^2 \text{ s}^{-1}$ in subsurface to slightly more than $4000 \text{ m}^2 \text{ s}^{-1}$
 487 around 1100 m depth, and then decreases to $3500 \text{ m}^2 \text{ s}^{-1}$ near the bottom.
 488 Note that subsurface (300-400 m) values are likely underestimates because,
 489 at these depths, the tracers rapidly spread along isopycnals up to the surface
 490 diabatic layer and then horizontally at the surface (see details in Appendix
 491 B). To obtain a more robust estimate near the surface, a set of 16 tracer
 492 patches were released right into the mixed layer, leading to an estimation
 493 of a surface (horizontal) diffusivity of about $1500 \text{ m}^2 \text{ s}^{-1}$; a slightly higher
 494 value than in subsurface which is more consistent with the other estimates.

495 To give a sense of the uncertainties, the diffusivities estimated from single
 496 tracer releases were also computed. The mean plus-or-minus one standard
 497 deviation of those 16 estimates (at each depth) are shown with a dashed
 498 black line and a light grey shading. Similarly, diffusivities from pairs of
 499 tracer releases were also computed (shown in dark grey shading and solid
 500 line). Uncertainties associated with a single tracer release range from ± 500
 501 $\text{m}^2 \text{ s}^{-1}$ near 500 m depth to $\pm 1000 \text{ m}^2 \text{ s}^{-1}$ or more below a 1000 m. It
 502 appears that estimates between 500 and 1000m deep would be somewhat

robust. However, our results suggest that detection of a peak of mixing in the water column would be very difficult from single tracer releases at a few selected depths.

5. Comparison of All Diagnostics

5.1. Averaging Method

In Sec. 3 we saw that many of the different perfect diagnostics (D'_{yy} , K_{eff}^{iso} , K_q and K_P) give similar results. Now we compare these results with the practical diagnostics discussed above. The central obstacle in this comparison is the question of how to average meridionally the perfect diagnostics, which are functions of y and z , to compare with the practical diagnostics, which are just functions of z . The tracers and particles for the practical experiments were released at the center of the domain and spread laterally along isopycnals for up to 300 days before encountering the boundaries. This results in a single value of diffusivity for each release depth, or equivalently, release isopycnal.² But as the particles / tracers experience spread away from the center of the channel, they experience weaker mixing towards the sides of the domain.

Our procedure is to average the perfect diagnostics in isopycnal bands of thickness ΔT over a meridional extent Δy , centered on the middle of the channel. Formally this average can be expressed as

$$\langle K \rangle(T_0) = \frac{1}{A} \int_{L_y - \Delta y/2}^{L_y + \Delta y/2} \int_{T(z)=T_0 - \Delta T/2}^{T(z)=T_0 + \Delta T/2} K dy dz \quad (22)$$

where T_0 is the target isopycnal and A is the cross-sectional area over which the integral is performed.³ ΔT effectively sets the vertical resolution of the averaged quantity, while Δy controls the width over which it samples. Larger Δy are associated with smaller $\langle K \rangle$, since the diffusivities tend to fall off away

²It would be possible in principle to calculate the practical diagnostics also as functions of y . But, in the spirit of simulating field experiments, we do not explore this possibility as it involves an even greater number of releases.

³Nakamura (2008) suggests that the proper way to average a spatially variable diffusivity is through a harmonic mean. We tested this, however, and found it to produce spurious results. This is because the harmonic mean is very sensitive to the presence of small values. Since our diffusivities are calculated numerically and contain some degree of noise at the grid scale, isolated small values can greatly influence the harmonic mean. For this reason, we prefer the simple arithmetic mean.

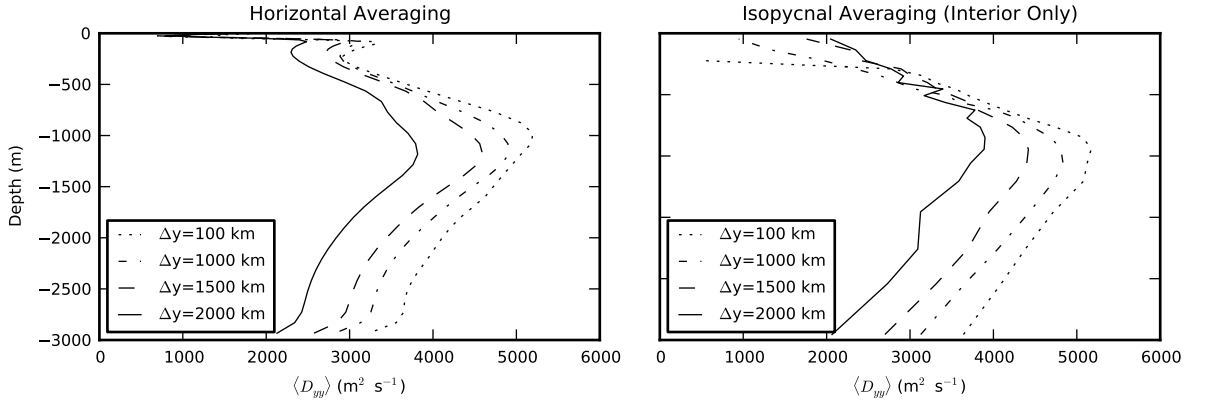


Figure 11: A comparison of meridional averages of D'_{yy} computed on surfaces of constant height (left panel) and isopycnal surfaces, with various averaging widths Δy . The average at constant height includes the whole domain, while the isopycnal average excludes the surface diabatic layer.

from the center of the channel. This effect is illustrated in Fig. 11, which shows $\langle D'_{yy} \rangle$ for different values of Δy . The figure also shows the difference between isopycnal averaging and simple horizontal averaging (i.e. averaging at constant z), which is a more straightforward way to produce depth profiles but is physically unsound. Instead, we map our profiles of $\langle K \rangle(T)$ to depth coordinates using the temperature profile $T(z)$ at the tracer and particle release latitude in the center of the domain.⁴

To fairly compare our diagnostics in the interior, we must exclude the surface diabatic layer from our average. This is because PV is not diffused down gradient in the surface layer due to the presence of strong forcing, which causes K_P to acquire negative values there (see Fig. 6). For this reason, we limit our isopycnally averaged diffusivities to the interior, which we define as the region below the 95% contour of $\bar{\Pi}$. The effect of excluding the surface layer can be seen in Fig. 11; the horizontal average, which includes the surface layer, shows a secondary peak near the surface, while the interior-only isopycnal average does not.

The choice of Δy clearly affects the magnitude of our averaged perfect

⁴On isopycnals which outcrop, the actual width of the averaging window may be considerably less than Δy . Furthermore, due to the sloping geometry of the isopycnals, the values of $\langle K \rangle$ near the surface are biased toward the northern side of the channel.

543 diagnostics. We have concluded that the optimum choice is $\Delta y = 1500$ m,
544 i.e. an average over the most of the domain, excluding the area closest to the
545 walls. This choice produced the best agreement between perfect and practical
546 diagnostics. It is also physically consistent with the fact that the particles
547 and tracers from the practical experiments spread out approximately over
548 this center portion of the channel (see Fig. 9).

549 5.2. Vertical Profile in the Interior

550 The values of $\langle D'_{yy} \rangle$, $\langle K_{eff}^{iso} \rangle$, $\langle K_P \rangle$ and $\langle K_b \rangle$ with $\Delta y = 1500$ m are all
551 plotted in Fig. 12. (K_q was not plotted because it is quite sparse and noisy
552 in the deep ocean. But Figs. 5 and 6 show that it is very similar to K_p .) Also
553 plotted are K_{1y} from the Lagrangian experiment and K_I from the tracer ex-
554 periment. There is fairly good agreement between the diagnostics, excluding
555 K_b . In particular, $\langle D'_{yy} \rangle$, $\langle K_{eff} \rangle$, and K_{1y} show very similar magnitudes and
556 vertical structure, with a distinct peak near 1000 m depth of approx. 4000
557 $m^2 s^{-1}$. K_P is qualitatively similar, with a sharp peak near the same depth,
558 but its magnitude at the peak ($5000 m^2 s^{-1}$) is greater. Then it drops off
559 steeply below this peak. (K_P is poorly resolved below 1000 m because it
560 is computed in isopycnal space; the deep is very weakly stratified, and thus
561 there are few layers defined there.) The profile of K_I shows a similar qual-
562 itative structure, but a slightly reduced magnitude above 1000 m compared
563 with the other diagnostics. In general, there is more spread between diag-
564 nostics in the deep ocean. The overall impression from this comparison is
565 that, despite the wide range of diagnostic methods and the ambiguities as-
566 sociated with the averaging process, all these diagnostics are capturing the
567 same physical process of along-isopycnal mixing in the interior. All, that is,
568 except K_b .

569 As discussed clearly in SM09, the diffusivities of buoyancy and potential
570 vorticity cannot be the same when β is significant, and when there is ver-
571 tical variation in the diffusivity profile. Nevertheless, the assumption that
572 these two quantities are equal continues to be made in eddy parameterization
573 schemes (for example Eden, 2010). Our results essentially confirm the conclu-
574 sions of SM09, who used a doubly-periodic QG model, in a primitive-equation
575 model with realistic meridional variations in stratification and residual cir-
576 culation. In particular, our Fig. 12 agrees well with their Fig. 12. While the
577 tracer, particle, and PV diffusivities all have a mid-depth peak, K_b does not;
578 instead it varies only weakly in the vertical. Its magnitude is less than half
579 that of K_P at the peak.

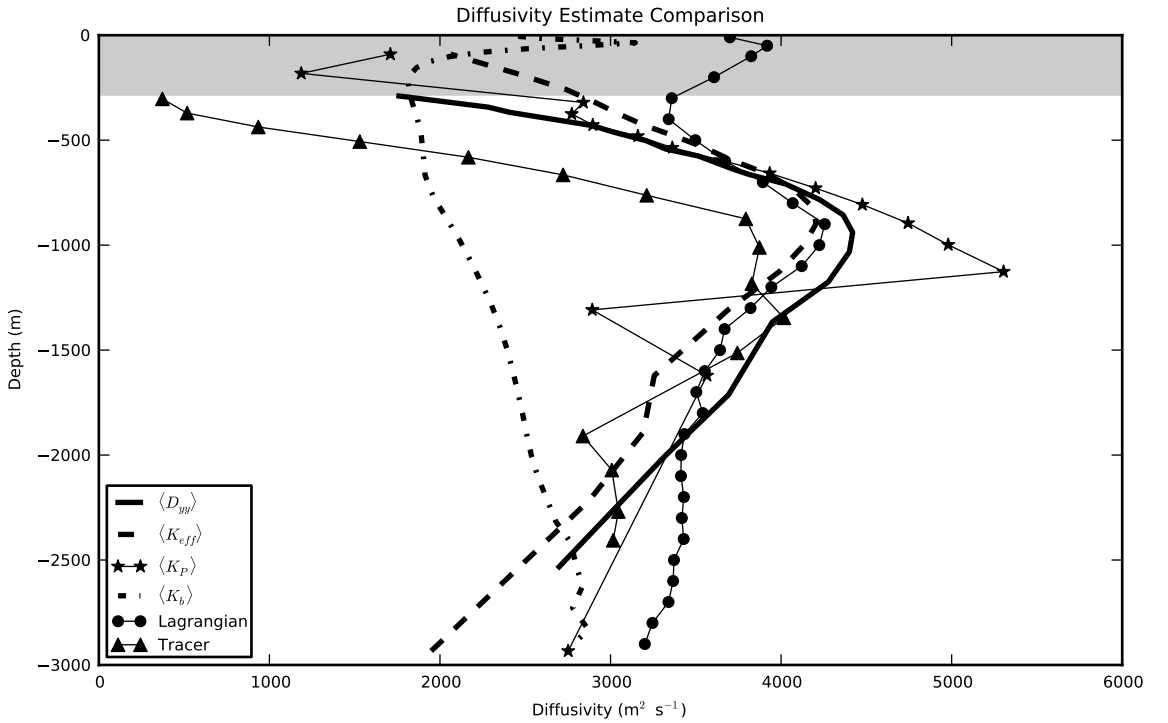


Figure 12: A comparison of all the different diffusivity diagnostics presented in the paper. For the perfect diagnostics, the meridional average was computed using (22) with a width of $\Delta y = 1500$ m, and only in the interior (outside the surface diabatic layer). The average depth of the SDL (280 m) is indicated by the gray shaded area.

580 Since the perfect diagnostics were averaged only in the interior, they
 581 do not show a secondary peak near the surface. This secondary peak is
 582 clearly visible in K_{1y} , the particle diffusivity. The average depth of the
 583 surface diabatic layer is also shown in Fig. 12. The secondary peak in K_{1y}
 584 clearly occurs within this surface layer. Since the surface is dynamically quite
 585 different from the interior, we now focus on the surface specifically.

586 5.3. Comparison at the Surface

587 Near the surface, eddies transition from isopycnal mixing to horizontal
 588 mixing across the surface buoyancy gradient (Treguier et al., 1997). This
 589 transition is visible in Fig. 3, which shows that the mixing angle becoming
 590 flatter near the surface and no longer aligns with the isopycnals. In Fig. 13,

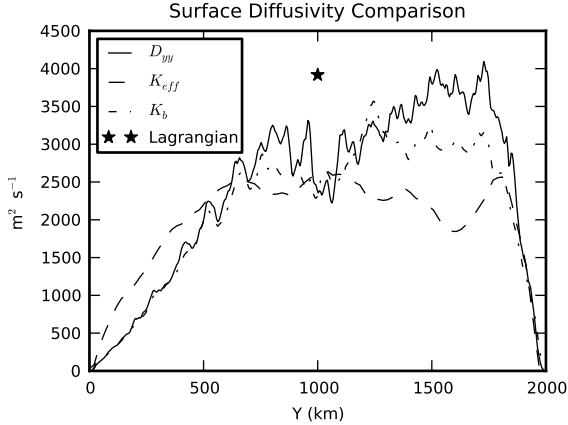


Figure 13: A comparison of D'_{yy} , K_{eff} and K_b at 50m depth.

we plot D'_{yy} , K_{eff}^H and K_b all at 50 m depth, near the base of the mixed layer. Also plotted is a single point representing K_{1y} . At the surface, we do indeed find better agreement between K_b and the other diagnostics. This is because the near-surface eddy buoyancy flux is truly down-gradient, as opposed to the interior where it is purely skew. Nevertheless, discrepancies remain, particularly near $Y = 1500$ km. We speculate that this is due to the differences in forcing and small-scale diffusivity among the three tracers. The tracer used to calculate K_{eff} was modeled with an explicit small-scale horizontal diffusion, while the others were not. Furthermore, the buoyancy is subject to an air-sea flux, which can strongly modulate the diffusivity. We have not attempted to quantify this effect here, but an in-depth treatment of the problem can be found in Shuckburgh et al. (2011).

6. Parameterization of Eddy Fluxes

One important motivation for understanding mixing rates is the goal of parameterizing eddy fluxes in coarse resolution models. A related goal is to use diffusive closures in conjunction with observed mean hydrography to infer eddy fluxes from observations, as done, for example, by Speer et al. (2000) or Sallée et al. (2008). Here we present two simple test cases that illustrate how our results apply to the parameterization problem.

First, we recall the conclusion from Sec. 5.2 that the perfect and practical diagnostics of mixing all pointed towards a consistent vertical profile of along-

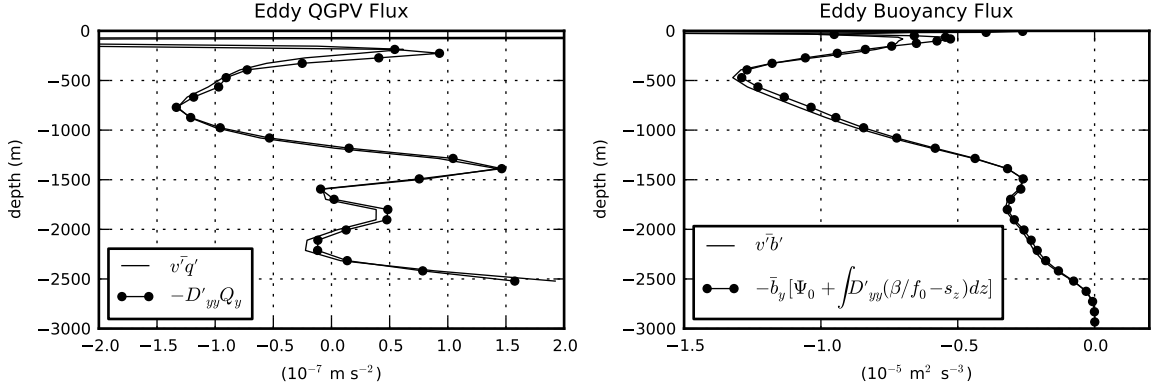


Figure 14: Estimates of the eddy QGPV flux (left) and buoyancy flux (right) made using D'_{yy} .

isopycnal mixing. A field experiment with sufficient Lagrangian floats could, in principle, measure D'_{yy} , the along isopycnal mixing rate. But once D'_{yy} has been determined, whether through observations, models, or theoretical arguments, what is the best way to make use of it for parameterization?

We have demonstrated that D'_{yy} is very similar to the diffusivity of potential vorticity. Therefore, the most direct closure is to parameterize the PV flux using D'_{yy} . In particular, the eddy QGPV flux is the basis of the parameterization proposed by Treguier et al. (1997) (see also Green, 1970; Marshall, 1981, 1984; Visbeck et al., 1997). We test the closure

$$\overline{v'q'} \simeq -D'_{yy}Q_y \quad (23)$$

by plotting the left and right sides of this equation in Fig. 14a. Clearly this closure is excellent for estimating the eddy QVPV flux. Unfortunately, ocean models do not commonly implement PV-based eddy closures due numerous practical obstacles, such as the need to enforce momentum conservation (see Marshall, 1981; Ferrari et al., 2010; Marshall et al., 2012, for further discussion).

A vastly more common approach is to parameterize the eddy buoyancy flux using an equation of the form $\overline{v'b'} = -K_b\bar{b}_y$, the so-called Gent-McWilliams closure (Gent and McWilliams, 1990; Gent et al., 1995; Griffies, 1998). Nearly all ocean models use some form of this closure, rather than one based on PV. But as discussed in Sec. 5.2, the buoyancy diffusivity K_b is quite different

632 from all the other diffusivities, including D'_{yy} . This is because the buoyancy
 633 flux is nearly completely skew in the interior and is not directly related to
 634 the along-isopycnal mixing rate. This leaves a frustrating dilemma for pa-
 635 rameterization: how can the measurable mixing rate, as expressed by D'_{yy} ,
 636 be used in a Gent-McWilliams closure scheme?

637 One possible answer is to use (13) to express the buoyancy flux in terms
 638 of the QGPV flux. Integrating (13) vertically, we find

$$\overline{v'b'} = \frac{1}{f_0} \bar{b}_z \left(\Psi_0 + \int_{-H}^z \overline{v'q'} dz' \right) \quad (24)$$

639 where Ψ_0 is an unknown constant of integration. Substituting (23) for the
 640 QGPV flux term and using the definition of Q_y from (14), we arrive at

$$\overline{v'b'} = \bar{b}_z \left[\Psi_0 - \int_{-H}^z D'_{yy} (\beta/f_0 - \frac{\partial s_b}{\partial z}) dz' \right]. \quad (25)$$

641 This expression provides a way to relate D'_{yy} to the buoyancy flux. We test
 642 it in Fig. 14a, using a value of $\Psi_0 = 4 \text{ m}^2 \text{ s}^{-1}$. The expression clearly works
 643 well, as evidenced by the strong agreement between the two curves in the
 644 figure. However, the success is compromised by the presence of the unknown
 645 constant Ψ_0 , which we have tuned here to give good agreement. Nevertheless,
 646 an expression of the form (25) could form the basis of future parameterization
 647 efforts. Additional discussion of the relationship between the eddy fluxes of
 648 QGPV and buoyancy can be found in SM09 (Sec. 4b).

649 7. Conclusions

650 Our paper has not derived any fundamentally new methods; rather, we
 651 have unified many different diagnostics of lateral mixing and applied them
 652 to the same simulation, permitting a side-by-side comparison. We have con-
 653 sidered both “perfect” diagnostics, which can realistically only be applied to
 654 a numerical model, as well as “practical” diagnostics, which can potentially
 655 be applied in field experiments. The results of this comparison are mostly
 656 summarized by Fig. 12, which shows appropriately averaged vertical profiles
 657 of lateral mixing rates as characterized by different diagnostics.

658 The encouraging conclusion is that these different methods for gauging
 659 along-isopycnal diffusivity produce good agreement. Despite differences in
 660 forcing, background state, initial conditions, and grid-scale diffusivity, we

661 found mixing rates for passive tracers, QGPV, and Ertel PV with similar
662 magnitude and spatial structure. This spatial structure includes higher mix-
663 ing rates in the center of the domain, where the eddies are stronger, and,
664 more intriguingly, a distinct mid-depth maximum in the vertical.

665 We have not gone into great detail on the explanation for this structure,
666 focusing instead on the details of the diagnostic methods themselves; how-
667 ever, the structure is well understood. Most theories for turbulent diffusivity
668 begin with the mixing-length concept of Prandtl (1925) (see, among many,
669 Green, 1970; Stone, 1972; Held and Larichev, 1996; Stammer, 1998; Smith
670 et al., 2002; Thompson and Young, 2007, for applications to geostrophic
671 turbulence). The recent literature contains a growing understanding of the
672 factors responsible for determining the isopycnal mixing rate in the South-
673 ern Ocean, and in particular the mid-depth peak. Beginning with Green
674 (1970), linear quasigeostrophic analysis has shown that the QGPV diffusiv-
675 ity must include a mid-depth maximum in unstable eastward flows (see also
676 Killworth, 1997). The work by Abernathey et al. (2010) showed that such a
677 mid-depth maxima did exist in a very realistic, eddy-permitting model of the
678 Southern Ocean and attributed its presence to a “critical layer,” at which
679 the eddy phase speed equaled the mean flow speed. Further work by Ferrari
680 and Nikurashin (2010), Klocker et al. (2012a), and Klocker et al. (2012b) has
681 confirmed this vertical structure and moved towards a complete theoretical
682 closure for the mixing rates. In the theory of Ferrari and Nikurashin (2010),
683 the competing effects of eddy kinetic energy, eddy size, eddy phase propa-
684 gation, and zonal mean flow all contribute to the diffusivity. The mid-depth
685 peak was interpreted as a result of strong suppression of mixing by the mean
686 flow at shallower depths.

687 Our results here, which show that isopycnal mixing rates are consistent
688 across a wide range of diagnostic methods, support the notion that the dif-
689 fusivity is a fundamental kinematic property of the flow. We hope these
690 results, obtained in a very simplified model, will encourage the community
691 to press on in the effort to measure isopycnal mixing observationally, relate
692 these measurements to theoretical models (such as Ferrari and Nikurashin,
693 2010), and apply this understanding to improving coarse-resolution models.
694 Indeed efforts are underway to translate the theoretical concepts outlined
695 above into a full-blown eddy closure scheme for ocean models (J. Marshall,
696 2013, personal communication).

697 At the same time, our study indicates some potential pitfalls that might
698 be encountered in attempting to relate observations of isopycnal mixing to

699 diagnostics from numerical models and to theoretical predictions. First of
700 all, there are significant uncertainties associated with practical mixing di-
701 agnostics. The errors associated with limited Lagrangian observations are
702 discussed by Klocker et al. (2012b). Here we have also addressed the er-
703 rors associated with limited isopycnal tracer release experiments (Sec. 4.2).
704 Furthermore, there is the problem that both these practical diagnostics in-
705 volve a spreading-out over large horizontal areas, experiencing different local
706 mixing rates along the way. This spreading means that the measured diffu-
707 sivities are biased lower than the peak diffusivity at the ACC core (Sec. 5.1).
708 This smoothing effect means that practical diagnostics are unlikely to be
709 able to detect, for instance, the fine-scale mixing barriers associated with the
710 multiple jets of the ACC (Thompson, 2010).

711 A final, crucial point is that the diffusivities measured by practical diag-
712 nostics can be used directly to estimate the eddy flux of potential vorticity
713 (either the lateral flux of QGPV or the along-isopycnal flux of Ertel PV). But
714 they can *not* be employed in a diffusive closure to recover the meridional eddy
715 buoyancy flux below the surface layer. This is because of the well-known fact
716 that the buoyancy flux is skew and is therefore not directly related to the
717 isopycnal diffusivity. A related point is that the isopycnal diffusivity is not
718 the same as K_b , the Gent-McWilliams transfer coefficient. We were able to
719 use the isopycnal diffusivity in (25) to reconstruct the meridional buoyancy
720 flux, but at the expense of introducing a free parameter.

721 Acknowledgements

722 We thank John Marshall, Baylor Fox-Kemper, and Malte Jansen for help-
723 ful suggestions.

724 Appendix A. Thickness-Weighted Isopycnal Averaging and the Er- 725 tel PV Flux

726 Analysis of flows in thickness-weighted isopycnal coordinates offers many
727 advantages in the ocean and atmosphere (Andrews et al., 1987; de Szoeke and
728 Bennett, 1993; Nurser and Lee, 2004b,a; Schneider, 2005; Koh and Plumb,
729 2004; Vallis, 2006; Jansen and Ferrari, 2012, 2013; Young, 2012; Mazloff et al.,
730 2013). Here we briefly repeat some definitions from Jansen and Ferrari (2013)
731 in order to derive the Ertel PV diffusivity.

732 In what follows, the vertical coordinate will be taken to be b , the buoy-
 733 ancy, and $z(x, y, z, b)$ is a dependent variable. All zonal averages are to be
 734 taken at constant b . The zonal- and time-averaged zonal momentum budget
 735 in b coordinates can be written as

$$-\overline{\mathcal{H}(b_s - b)fv} = -\overline{\mathcal{H}(b_s - b)\partial_x M} + \overline{\mathcal{H}(b - b_s)\mathcal{F}^x} \quad (\text{A.1})$$

736 where $M = p/\rho_0 - zb$ (the Montgomery potential) and \mathcal{F}^x is the forcing in
 737 the zonal direction. $\mathcal{H}(b_s - b)$ is a Heaviside function which is zero whenever
 738 the buoyancy surface outcrops, (i.e. when b exceeds the surface buoyancy
 739 b_s).

The importance of PV fluxes can be seen by writing the Coriolis term on the LHS as

$$\overline{\mathcal{H}(b_s - b)fv} = \overline{\rho_b v P^*} \quad (\text{A.2})$$

$$= \overline{\rho_b} (\overline{v^* P^*} + \overline{\hat{v} \hat{P}^*}). \quad (\text{A.3})$$

740 To arrive at this expression, we have defined the Ertel PV $P = f/\sigma$ (ne-
 741 glecting relative vorticity, appropriate for low Rossby number), the isopycnal
 742 thickness $\sigma = \partial z / \partial b$, the generalized thickness $\rho_b = \mathcal{H}(b_s - b)\sigma$, and the
 743 generalized thickness weighted zonal average $(\cdot)^* = \rho_b(\cdot)/\overline{\rho_b}$. (See Koh and
 744 Plumb (2004) or Jansen and Ferrari (2013) for more detail.) In the second
 745 line, the PV flux term $\overline{v P^*}$ is split into mean and eddy components; the
 746 anomalies are defined by $(\hat{\cdot}) = (\cdot) - (\cdot)^*$.

747 In the interior of our channel model, both terms on the RHS of (A.3)
 748 vanish. This permits us to write

$$\overline{v^*} = -\frac{\overline{\hat{v} \hat{P}^*}}{\overline{P^*}}, \quad (\text{A.4})$$

749 The quantity $\overline{v^*}$, the thickness-weighted mean meridional velocity, is analo-
 750 gous to the residual velocity v_{res} in QG.

751 Appendix B. Tracer Release Experiments

752 As discussed in Hill et al. (2012), mimicking tracer release experiments in
 753 an ocean model can be problematic. One wants the initial tracer distribution
 754 to be as compact as possible (to be close to an isopycnal) but not too small
 755 compared to the grid scale. Also, the initial distribution has to be small

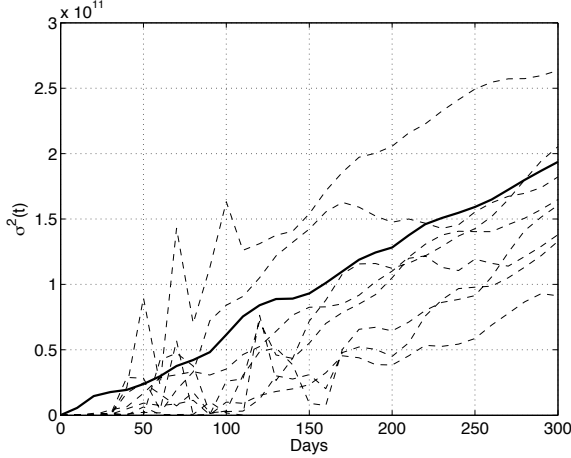


Figure B.15: Time evolution of σ^2 for each individual tracer release experiment (dashed lines) and for the 16-member ensemble (thick solid line) at 1200 m depth. Linear growth with time signifies a constant diffusivity.

enough, relative to the domain, to leave ample time before the tracer is transported into the surface mixed layer or north/south boundaries.

As a compromise (following Hill et al. (2012)), the tracer field is initialized with a 3D Gaussian shape with 50 m vertical and 5 km horizontal half-width. The tracer has a maximum value of one. We carried out 16 releases at 11 depths (shown by the open circles in Fig. 10). Each set of 16 releases consists of eight releases, 125 km apart along the central axis of the channel followed by a second set of eight 300 days later. The 3d tracer distributions are sampled every 10 days for 300 days. In order to calculate the isopycnal diffusivity, all vertical profiles are first plotted around a relative vertical coordinate centered on the target temperature of the release and then summed up vertically and zonally to produce a meridional profile. A Gaussian curve is fitted to the reconstructed meridional profile (from a single tracer or averaged from an ensemble of profiles, see examples in Fig. 9, bottom panels).

The best-fit half-width $\sigma_y(t)$ relates to the effective diffusivity through:

$$K_I = \frac{1}{2} \frac{d\sigma_y^2}{dt}. \quad (\text{B.1})$$

Fig. B.15 illustrates the time evolution of $\sigma_y(t)$ for a few single tracers (dashed lines) and for the 16-member ensemble mean (thick solid) for releases at 1200 m depth. The initial behavior of sigma is rather erratic for individual tracers,

774 but often approach a linear tendency after 150 days. The ensemble mean
775 value is very nearly linear from the tracer release onward. Note that this is
776 not true at all depths—in some cases the ensemble mean value only settles
777 down into a linear trend after a 100 days. For consistency, all isopycnal
778 diffusivities shown here are obtained by a best linear fit of $\sigma^2(t)$ between
779 1500 and 300 days.

780 Although $\sigma_y(t)$ from individual tracers exhibits rather similar trends after
781 \sim 150 days, the differences in slopes are sufficient to result in large uncertainties
782 on K_I , as much as $\pm 1500 \text{ m}^2 \text{ s}^{-1}$ at 1200 m.

783 References

- 784 Abernathey, R., Marshall, J., Ferreira, D., 2011. The dependence of southern
785 ocean meridional overturning on wind stress. *J. Phys. Oceanogr.* 41 (12),
786 2261–2278.
- 787 Abernathey, R., Marshall, J., Shuckburgh, E., Mazloff, M., 2010. Enhancement
788 of mesoscale eddy stirring at steering levels in the southern ocean. *J.
789 Phys. Oceanogr.*, 170–185.
- 790 Andrews, D., Holton, J., Leovy, C., 1987. Middle Atmosphere Dynamics.
791 Academic Press.
- 792 Bryden, H. L., Longworth, H. R., Cunningham, S. A., 2005. Slowing of the
793 atlantic meridional overturning circulation at 25° n. *Nature* 438, 655–657.
- 794 Cerovecki, I., Marshall, J., 2008. Eddy modulation of air–sea interaction and
795 convection. *J. Phys. Oceanogr.* 38, 65–93.
- 796 Cunningham, S. A., Kanzow, T., Rayner, D., Baringer, M. O., Johns, W. E.,
797 Marotzke, J., Longworth, H. R., Grant, E. M., Hirschi, J. J., Beal, L. M.,
798 Meinen, C. S., Bryden, H. L., 2007. Temporal variability of the atlantic
799 meridional overturning circulation at 26.5°n. *Science* 317 (5840), 935–938.
- 800 Davis, R., 1985. Drifter observations of coastal surface currents during
801 CODE: The statistical and dynamical views. *J. Geophys. Res.* 90, 4756–
802 4772.
- 803 Davis, R., 1991. Observing the general circulation with floats. *Deep Sea Res.*
804 38A, S531–S571.

- 805 Davis, R., 1994. Ocean Processes in Climate Dynamics: Global and Mediter-
806 ranean Examples. Springer, Ch. Lagrangian and Eulerian measurements
807 of ocean transport processes, pp. 29–60.
- 808 de Szoeke, R. A., Bennett, A. F., 1993. Microstructure fluxes across density
809 surfaces. *J. Phys. Oceanogr.* 23 (10), 2254–2264.
- 810 Eden, C., 2010. Parameterising meso-scale eddy momentum fluxes based on
811 potential vorticity mixing and a gauge term. *Ocean Modelling* 32, 58–71.
- 812 Ferrari, R., Griffies, S. M., Nurser, A. J., Vallis, G. K., 2010. A boundary-
813 value problem for the parameterized mesoscale eddy transport. *Ocean*
814 *Modelling*.
- 815 Ferrari, R., Nikurashin, M., 2010. Suppression of eddy diffusivity across jets
816 in the southern ocean. *J. Phys. Oceanogr.*
- 817 Fox-Kemper, B., Lumpkin, R., Bryan, F. O., 2012. Lateral transport in the
818 ocean interior. In: Siedler, G., Church, J., Gould, J., Griffies, S. (Eds.),
819 *Ocean Circulation and Climate – Observing and Modelling the Global*
820 *Ocean*. Elsevier.
- 821 Gent, P., McWilliams, J., 1990. Isopycnal mixing in ocean circulation models.
822 *J. Phys. Oceanogr.* 20, 150–155.
- 823 Gent, P., Willebrand, J., McDougal, T., McWilliams, J., 1995. Parameter-
824 izing eddy-induced tracer transports in ocean circulation models. *J. Phys.*
825 *Oceanogr.* 25, 463–475.
- 826 Gille, S. T., Ledwell, J., Naveira Garabato, A., Speer, K., Balwada, D.,
827 Brearley, A., Girton, J. B., Griesel, A., Ferrari, R., Klocker, A., LaCasce,
828 J., Lazarevich, P., Mackay, N., Meredith, M. P., Messias, M.-J., Owens, B.,
829 Sallée, J.-B., Sheen, K., Shuckburgh, E., Smeed, D. A., Laurent, L. C. S.,
830 Toole, J. M., Watson, A. J., Wienders, N., , Zajaczkowski, U., 2012. The
831 diapycnal and isopycnal mixing experiment: A first assessment. *CLIVAR*
832 *Exchanges* 17 (1), 46–48.
- 833 Green, J. S. A., 1970. Transfer properties of the large-scale eddies and the
834 general circulation of the atmosphere. *Quart. J. Roy. Meteor. Soc.* 96, 157–
835 185.

- 836 Griffies, S. M., 1998. The Gent-McWilliams skew flux. *J. Phys. Oceanogr.*
837 28, 831–841.
- 838 Haynes, P., Shuckburgh, E., 2000a. Effective diffusivity as a diagnostic of
839 atmospheric transport. part i: stratosphere. *J. Geophys. Res* 105, 22777–
840 22794.
- 841 Haynes, P., Shuckburgh, E., 2000b. Effective diffusivity as a diagnostic of
842 atmospheric transport. part ii: Troposphere and lower stratosphere. *J.*
843 *Geophys. Res* 105, 795–810.
- 844 Held, I. M., Lariehev, V. D., 1996. A scaling theory for horizontally homoge-
845 neous, baroclinically unstable flow on a beta plane. *J. Atmos. Sci.* 53 (7),
846 946–953.
- 847 Hill, C., Ferreira, D., Campin, J.-M., Marshall, J., Abernathey, R., Barrier,
848 N., 2012. Controlling spurious diapycnal mixing in eddy-resolving height-
849 coordinate ocean models: Insights from virtual deliberate tracer release
850 experiments. *Ocean Modelling* 45-46, 14–26.
- 851 Ito, T., Marshall, J., 2008. Control of lower-limb overturning circulation in
852 the southern ocean by diapycnal mixing and mesoscale eddy transfer. *J.*
853 *Phys. Oceanogr.* 38, 2832–2845.
- 854 Jansen, M., Ferrari, R., 2012. Macroturbulent equilibration in a thermally
855 forced primitive equation system. *J. Atmos. Sci.*
- 856 Jansen, M., Ferrari, R., 2013. The vertical structure of the eddy diffusivity
857 and the equilibrarion of the extra-tropical atmosphere. *J. Atmos. Sci.*
- 858 Killworth, P. D., 1997. On the parameterization of eddy transfer: Part i:
859 Theory. *J. Marine Res.* 55, 1171–1197.
- 860 Klocker, A., Ferrari, R., LaCasce, J. H., 2012a. Estimating suppression of
861 eddy mixing by mean flow. *J. Phys. Oceanogr.* 9, 1566–1576.
- 862 Klocker, A., Ferrari, R., LaCasce, J. H., Merrifield, S. T., 2012b. Reconcil-
863 ing float-based and tracer-based estimates of eddy diffusivities. *J. Marine*
864 *Res.* Submitted.
- 865 Koh, T., Plumb, R. A., 2004. Isentropic zonal average formalizm and the
866 near-surface circulation. *Q. G. R. Meteorol. Soc.* 130, 1631–1653.

- 867 Kuo, A., Plumb, R. A., Marshall, J., 2005. Transformed eulerian-mean the-
868 ory. part ii: Potential vorticity homogenization and equilibrium of a wind-
869 and buoyancy-driven zonal flow. *J. Phys. Oceanogr.* 45, 175–187.
- 870 LaCasce, J. H., 2008. Statistics from lagrangian observations. *Progress in*
871 *Oceanography* 77, 1–29.
- 872 Ledwell, J. R., Bratkovich, A., 1995. A tracer study of mixing in the santa
873 cruz basin. *J. Geophys. Res.* 100 (C10), 20,681.
- 874 Ledwell, J. R., St. Laurent, L. C., Girton, J. B., 2011. Diapycnal mixing in
875 the Antarctic Circumpolar Current. *J. Phys. Oceanogr.* 41 (241-246).
- 876 Ledwell, J. R., Watson, A. J., Law, C. S., 1998. Mixing of a tracer in the
877 pycnocline. *J. Geophys. Res.* 103 (C10), 21,499–21,592.
- 878 Liu, C., Köhl, A., Stammer, D., 2012. Adjoint based estimation of eddy
879 induced tracer mixing parameters in the global ocean. *J. Phys. Oceanogr.*
880 42, 1186–1206.
- 881 Lu, J., Speer, K., 2010. Topography, jets, and eddy mixing in the southern
882 ocean. *J. Marine Res.* 68 (479-502).
- 883 Lumpkin, R., Speer, K., 2007. Global meridional overtuning. *J. Phys.*
884 *Oceanogr.* 37, 2550–2537.
- 885 Marshall, D. P., Maddison, J. R., Berloff, P. S., 2012. A framework for pa-
886 rameterizing eddy potential vorticity fluxes. *J. Phys. Oceanogr.*
- 887 Marshall, J., 1981. On the parameterization of geostrophic eddies in the
888 ocean. *J. Phys. Oceanogr.* 11, 1257–1271.
- 889 Marshall, J., 1984. Eddy-mean-flow interaction in a barotropic ocean model.
890 *Q. G. R. Meteorol. Soc.* 110, 573–580.
- 891 Marshall, J., Adcroft, A., Hill, C., Perelman, L., Heisey, C., 1997a. A finite-
892 volume, incompressible navier stokes model for studies of the ocean on
893 parallel computers. *J. Geophys. Res.* 102, 5753–5766.
- 894 Marshall, J., Hill, C., Perelman, L., Adcroft, A., 1997b. Hydrostatic, quasi-
895 hystrostatic, and non-hydrostatic ocean modeling. *J. Geophys. Res.* 102,
896 5733–5752.

- 897 Marshall, J., Radko, T., 2003. Residual mean solutions for the antarctic
898 circum polar current and its associated overturning circulation. *J. Phys.*
899 *Oceanogr.* 33, 2341–2354.
- 900 Marshall, J., Shuckburgh, E., Jones, H., Hill, C., 2006. Estimates and im-
901 plications of surface eddy diffusivity in the southern ocean derived from
902 tracer transport. *J. Phys. Oceanogr.* 36, 1806–1821.
- 903 Marshall, J., Shutts, G., 1981. A note on rotational and divergent eddy fluxes.
904 *J. Phys. Oceanogr.* 21, 1677–1681.
- 905 Marshall, J., Speer, K., 2012. Closing the meridional overturning circulation
906 through southern ocean upwelling. *Nature Geoscience* 5, 171–180.
- 907 Mazloff, M., Ferrari, R., Schneider, T., 2013. he force balance of the southern
908 ocean meridional overturning circulation. *J. Phys. Oceanogr.*
- 909 Nakamura, N., 1996. Two-dimensional mixing, edge formation, and perme-
910 ability diagnosed in an area coordinate. *J. Atmos. Sci.* 53, 1524–1537.
- 911 Nakamura, N., 2001. A new look at eddy diffusivity as a mixing diagnostic.
912 *J. Atmos. Sci.* 58, 3685–3702.
- 913 Nakamura, N., 2008. Quantifying inhomogeneous, instantaneous, irreversible
914 transport using passive tracer field as a coordinate. *Lect. Notes Phys* 744,
915 137–164.
- 916 Nakamura, N., Ma, J., 1997. Modified lagrangian-mean diagnostics of the
917 stratospheric polar vortices 2. nitrous oxide and seasonal barrier migra-
918 tion in the cryogenic limb array etalon spectrometer and skyhi general
919 circulation model. *J. Geophys. Res.* 102, 25,721–25,735.
- 920 Naveira-Garabato, A. R., Ferrari, R., Polzin, K., 2011. Eddy stirring in the
921 southern ocean. *J. Geophys. Res.* 116, C09019.
- 922 Nikurashin, M., Vallis, G., 2012. A theory of the interhemispheric meridional
923 overturning circulation and associated stratification. *J. Phys. Oceanogr.*
- 924 Nurser, A. J., Lee, M.-M., 2004a. Isopycnal averaging at constant height. part
925 i: Relating to residual streamfunction. *J. Phys. Oceanogr.* 34 (2740-2755).

- 926 Nurser, A. J., Lee, M.-M., 2004b. Isopycnal averaging at constant height. part
927 i: The formulation and a case study. *J. Phys. Oceanogr.* 34 (2721–2739).
- 928 Plumb, R. A., 1979. Eddy fluxes of conserved quantities by small-amplitude
929 waves. *J. Atmos. Sci.* 36, 1699–1705.
- 930 Plumb, R. A., Ferrari, R., 2005. Transformed eulerian-mean theory. part
931 i: Nonquasigeostrophic theory for eddies on a zonal-mean flow. *J. Phys.*
932 *Oceanogr.* 35, 165–174.
- 933 Plumb, R. A., Mahlman, J. D., 1987. The zonally-averaged transport char-
934 acteristics of the gfdl general circulation/tracer model. *J. Atmos. Sci.* 44,
935 298–327.
- 936 Prandtl, L., 1925. Bericht untersuchungen zur ausgebildeten turbulenz. *Zs.*
937 *angew. Math. Mech.* 5, 136–139.
- 938 Prather, M. J., 1986. Numerical advection by conservation of second-order
939 moments. *J. Geophys. Res.* 91 (D6), 6671–6681.
- 940 Rhines, P. B., Young, W. R., 1982. Homogenization of potential vorticity in
941 planetary gyres. *J. Fluid Mech.* 122, 347–367.
- 942 Sallée, J. B., Speer, K., Morrow, R., Lumpkin, R., 2008. An estimate of
943 lagragian eddy statistics and diffusion in the mixed layer of the southern
944 ocean. *J. Marine Res.* 66 (4), 441–463.
- 945 Sallée, J. B., Speer, K., Rintoul, S., Wijffels, S., 2010. Southern ocean ther-
946 mocline ventilation. *J. Phys. Oceanogr.* 40, 509–530.
- 947 Sarmiento, J. L., Toggweiler, J. R., 1984. A new model for the role of the
948 oceans in determining atmospheric pco₂. *Nature* 308, 621–624.
- 949 Schneider, T., 2005. Zonal momentum balance, potential vorticity dynamics,
950 and mass fluxes on near-surface isentropes. *J. Atmos. Sci.* 62, 1884–1900.
- 951 Shuckburgh, E., Jones, H., Marshall, J., Hill, C., 2009a. Robustness of effec-
952 tive diffusivity diagnostic in oceanic flows. *J. Phys. Oceanogr.* 39, 1993–
953 2009, in Press.

- 954 Shuckburgh, E., Jones, H., Marshall, J., Hill, C., 2009b. Understanding the
955 regional variability of eddy diffusivity in the pacific sector of the southern
956 ocean,. *J. Phys. Oceanogr.* 39, 2011–2023, in Press.
- 957 Shuckburgh, E., Maze, G., Ferreira, D., Marshall, J., Jones, H., Hill, C.,
958 2011. Mixed layer lateral eddy fluxes mediated by air-sea interaction. *J.*
959 *Phys. Oceanogr.* 41, 130–144.
- 960 Sigman, D., Boyle, E., 2000. Glacial/interglacial variations in atmospheric
961 carbon dioxide. *Nature* 407 (6806), 859–869.
- 962 Smith, K. S., Boccaletti, G., Henning, C. C., Marinov, I., Tam, C. Y., Held,
963 I. M., Vallis, G. K., 2002. Turbulent diffusion in the geostrophic inverse
964 cascade. *J. Fluid Mech.* 469, 13–48.
- 965 Smith, K. S., Marshall, J., 2009. Evidence for enhanced eddy mixing at mid-
966 depth in the southern ocean. *J. Phys. Oceanogr.* 39, 50–69.
- 967 Speer, K., Rintoul, S., Sloyan, B., 2000. The diabatic deacon cell. *J. Phys.*
968 *Oceanogr.* 30, 3212–3223.
- 969 Stammer, D., 1998. On eddy characteristics, eddy transports, and mean flow
970 properties. *J. Phys. Oceanogr.* 28, 727–739.
- 971 Stone, P. H., 1972. A simplified radiative-dynamical model for the static
972 stability of rotating atmospheres. *J. Atmos. Sci.* 29 (3), 405–417.
- 973 Taylor, G. I., 1921. Diffusion by continuous movements. *Proc . London Math.*
974 *Soc.* s2-20, 196–212.
- 975 Thompson, A. F., 2010. Jet formation and evolution in baroclinic turbulence
976 with simple topography. *J. Phys. Oceanogr.* 40, 257–274.
- 977 Thompson, A. F., Young, W. R., 2007. Two-layer baroclinic eddy heat fluxes:
978 Zonal flows and energy balance. *J. Atmos. Sci.* 64, 3214–3232.
- 979 Treguier, A. M., 1999. Evaluating eddy mixing coefficients from eddy-
980 resolving ocean models: A case study. *J. Marine Res.* 57, 89–108.
- 981 Treguier, A. M., Held, I., Larichev, V., 1997. Parameterization of quasi-
982 geostrophic eddies in primitive equation ocean models. *J. Phys. Oceanogr.*
983 27, 567–580.

- 984 Vallis, G., 2006. Atmospheric and Oceanic Fluid Dynamics. Cambridge Uni-
985 versity Press.
- 986 Visbeck, M., Marshall, J., Haine, T., 1997. Specification of eddy transfer co-
987 efficients in coarse-resolution ocean circulation models. *J. Phys. Oceanogr.*
988 27, 381–403.
- 989 Wilson, C., Williams, R. G., 2004. Why are eddy fluxes of potential vorticity
990 difficult to parameterize? *J. Phys. Oceanogr.* 34, 142–155.
- 991 Winters, K., D'Asaro, E., 1996. Diascalar flux and the rate of fluid mixing.
992 *J. Fluid Mech.* 317, 179–193.
- 993 Wunsch, C., 2008. Mass and volume transport variability in an eddy-filled
994 ocean. *Nature Geoscience* 1, 165–168.
- 995 Young, W. R., 2012. An exact thickness-weighted average formulation of the
996 boussinesq equations. *J. Phys. Oceanogr.*